Production of K^0_S and Λ in p-Pb Collisions at $\sqrt{s_{NN}} = 5.02$ TeV Measured with the ALICE Detector at the LHC

Master's Thesis
by
Madeleine Burheim

Supervisor:
David Silvermyr

Abstract

This thesis presents an analysis of the production of K^0_S and Λ particles in p-Pb collisions at a center of mass collision energy of $\sqrt{s_{NN}} = 5.02$ TeV, measured with the ALICE detector at the LHC, CERN. The p_T spectra as well as the baryon-to-meson yield ratio Λ/K^0_S, for $p_T \leq 15$ GeV/c, are investigated and compared for different centrality bins. The results are compared to those from Pb-Pb collisions, where the yield ratio shows pp-like behaviors for peripheral collisions while for central collisions an enhancement of Λ with respect to K^0_S is seen at intermediate p_T. This enhancement is, to our current knowledge, explained by effects of radial flow at low and mid-p_T combined with processes like recombination during the hadronization of the created medium – the Quark Gluon Plasma. The results of p-Pb show similar features to those of Pb-Pb, but on a smaller scale.

LUND UNIVERSITY

Division of Particle Physics
Department of Physics
Lund University

Populärvetenskaplig sammanfattning

Många har hört talas om *The Big Bang* – den stora smällen – det ögonblick där det Universum som vi känner till idag föddes. Även om vad som fanns innan Big Bang ännu förblir en gåta, tyder observationer på att alla galaxer, stjärnor och planeter som idag existerar – även rumtiden själv – började i en enda punkt. Denna punkt måste ha varit oerhört tät och het, vilket innebär att den materien vi ser runt omkring oss idag, som är uppbyggd av den bekanta atomen, inte kunde existera. Då Universum bara var några miljondelar av en sekund gammalt, fanns det inte ens protoner eller neutroner – de beståndsdelar som bygger upp atomkärnor.

Istället tros en annan typ av materia ha existerat; en materia uppbyggd av fria kvarkar och gluoner, d.v.s. de partiklar som, under normala förhållanden (vid låg densitet och temperatur), är bundna i hadroner – en grupp partiklar dit protoner och neutroner tillhör. Ett sådant materietillstånd kallas för *kvark-gluonplasma* (QGP).

Då Universum expanderade, och därigenom kyldes ned, ledde detta till att kraften mellan partiklarna i kvark-gluonplasmat – den så kallade starka kraften – blev allt större. Denna kraft fungerar så, att den minskar då partiklarna kommer nära varandra och ökar när de förs längre ifrån varandra. Och skulle det vara så att två kvarkar av någon anledning kommer för långt ifrån varandra, så omvandlas den energin som håller ihop kvarkarna till att bilda ett nytt kvarkpar som de ursprungliga kvarkarna istället kan bindas till. Detta beteende hos den starka kraften innebär att kvarkarna och gluonerna aldrig existerar som fria partiklar. Då Universum fortsatte kylas ned började dessa partiklar därför smälta samman för att bilda hadroner.

Genom kollisioner mellan tunga atomkärnor – såsom blykärnor (Pb) – accelererade till en hastighet nära ljushastigheten, kan så höga temperaturer och tryck uppnås att kvarkarna och gluonerna i den sammanpressade materien beter sig som fria partiklar. Detta innebär att den hadroniska materien har genomgått en fasövergång till det särskilda materietillståndet QGP.

Då avkylningen av den skapade materien går så snabbt, går det inte att direkt mäta på kvark-gluonplasmat självt. Istället måste man analysera de partiklar som produceras i processen. De kärnor som kolliderar innehåller protoner och neutroner, vilka endast är uppbyggda av två sorters kvarkar. Trots det har partiklar som innehåller andra sorters kvarkar upptäckts, vid sådana kollisioner, i en mängd som inte har observerats i situationer där kvark-gluonplasma inte förväntas bildas – t.ex. vid kollisioner mellan två protoner.

Vad blir då resultatet när man kolliderar protoner med tunga kärnor? I min avhandling undersöker jag just detta, nämligen vad som händer i kollisioner mellan protoner och Pb-kärnor. De data som min analys baseras på kommer från proton-Pb-kollisioner uppmätta med ALICE-detektorn vid LHC (Large Hadron Collider), CERN. I analysen undersöker jag två sorters partiklar, K_S^0 och Λ, som bildads i kollisionerna och hur dess antal förhåller sig till varandra beroende på kollisionens centralitet (var på kärnan som protonen träffar). Antalet undersöks i förhållande till partiklarnas rörelsemängd, vilket sedan jämförs med motsvarande resultat från Pb-Pb-kollisioner, där QGP har observerats.

Acknowledgments

First and foremost, I would like to thank my supervisor David Silvermyr for proposing this very interesting topic and, together with co-supervisor Peter Christiansen, guiding me throughout the course of my thesis. I want to thank Anders Oskarsson for helping me in preparation for the DQM shifts at ALICE, as well as everyone involved in giving me the opportunity to go there.

I also want to give a special thanks to Tuva Richert, Martin Ljunggren and Vytautas Vislavičius for being there for me when extra help was needed and, together with the rest of my co-workers, always creating a great atmosphere in the office.

Finally, I would like to say thank you to everyone in the Lund Particle Physics division for a truly memorable year and to all the people involved for making this happen!

Madeleine

Contents

1 Introduction

1.1 The aim of the study

Through collisions of heavy ions, it has been discovered that quarks and gluons are able to move around as free particles and no longer bound in hadrons; a highly dense state of matter called *Quark Gluon Plasma* (QGP). The QGP is believed to have existed in the early Universe – a few microseconds after the Big Bang – and as the Universe cooled down and expanded the quarks and gluons grouped together to form hadrons (such as protons and neutrons).

In the beginning of heavy-ion physics this medium was thought to be created only in the collisions between two heavy nuclei – such as lead (Pb) nuclei. Recently, however, behaviors similar to those of QGP have also been found when protons are collided with Pb ions. The aim of this analysis is, thus, to investigate the features of QGP in p-Pb collisions. In the analysis this is done by examining the yields of two kinds of particles created in the collisions; the K^0_S meson and the Λ baryon. These particles are commonly referred to as V^0 particles, since they are both neutral (i.e. they carry no electromagnetic charge) and their decays products leave a V-shaped trail in the detector.

The results of the analysis are presented as distributions of transverse momentum (p_T), where the yield (number of particles) for a given p_T can be derived. By comparing the yields of particles of different mass (such as the K^0_S and Λ), certain characteristics of the QGP are made apparent.

The questions this thesis aspires to answer are: How do the yields of the two particles in question relate to each other in the case of p-Pb collisions? How does this relationship change for different collision centralities? How do these results compare to those obtained from pp and Pb-Pb collisions?

In order to answer these questions the signals from the V^0 invariant mass distributions have to be extracted. This, I do by adding some conditions (cuts) on the V^0 reconstruction after which I perform a background subtraction to remove unwanted contributions to the spectra.

1.2 Layout of the thesis

This thesis is divided into six sections. Section 2 provides a short description of the Standard Model of particle physics, where the different particles and how they interact with each other is discussed. The Quark Gluon Plasma and some of its features is introduced in Sec. 3, where in Sec. 3.2 some concepts that will be useful for the rest of the thesis are presented. In Sec. 4 a brief presentation of the ALICE experiment and the detectors is given where Sec. 4.1.5 gives a summary of the detectors that have been used for the collecting the data used in this analysis. The analysis itself is presented and discussed in Sec. 5 where results from the Monte Carlo study are given in Sec. 5.3 and the real data analysis is introduced in Sec. 5.6. Finally, the results from the data analysis are presented and discussed in Sec. 6, where they are compared to published results from ALICE.

2 The Theory of Particle Physics

2.1 The Standard Model

The Standard Model (SM) of particle physics describes the fundamental particles, the basic building blocks of all matter, and how they interact. Today's SM includes three of the four fundamental forces of nature (gravity being the fourth one) – the electromagnetic force, the weak force and the strong force. The electromagnetic force is described by the theory of Quantum Electrodynamics (QED) and for high enough energies, the weak and electromagnetic forces unify to form the *electroweak force*. Physicists have so far not been able to verify any unification between the strong force, which is described by the theory of Quantum Chromodynamics (QCD), and the electroweak force. The three forces of the SM are the result of the exchange of force-carrier particles, called *gauge bosons*.

2.1.1 The Fermions

The elementary particles can be separated into fermions and bosons, depending on if they have half-integer or integer spin, respectively. The fermions are in turn divided into to subgroups – quarks and leptons – which both have the characteristic spin 1/2. The charged leptons, i.e. the electron (e^-), muon (μ^-), and tau (τ^-), carry an electric charge of -e and each of them has a corresponding neutrino – the electron neutrino (ν_e), muon neutrino (ν_μ), and tau neutrino (ν_τ). The neutrinos are electrically neutral and nearly massless. While the neutral leptons can only interact weakly, the electrically charged leptons interact both weakly and electromagnetically.

As of today, there are six known quarks – each with a specific flavor, up (u), down (d), charm (c), strange (s), top (t), and bottom (b). The up, charm, and top quarks carry an electric charge of $2/3e$, while the down, strange, and bottom quarks have charge -$1/3e$. Apart from electric charge, quarks carry color charge. A quark can thus take one of three colors[1]; red, green, or blue. Since color charge is a property of QCD, this means that quarks can also interact strongly. Antiquarks carry the corresponding anti-colors.

2.1.2 The Gauge Bosons

Apart from fermions, the Standard Model also includes (gauge) bosons, which have integer spin. These are the so-called mediators (or force carriers) of the three forces mentioned above. The known gauge bosons are the photon (γ), which mediates the electromagnetic force, the Z^0, $W^\pm$, which mediate the weak force, and the gluon, the mediator of the strong force. The photon is a massless boson, which gives rise to the infinite range of the electromagnetic force. The weak force is, as the name implies, the weakest force in the Standard Model and due to its heavy mediators also has the shortest range.

[1]Color here does not refer to the visual perception of color. The fact that three quarks have to form a "color neutral" state inside a baryon, however, resembles the way the three primary colors combine to create white light.

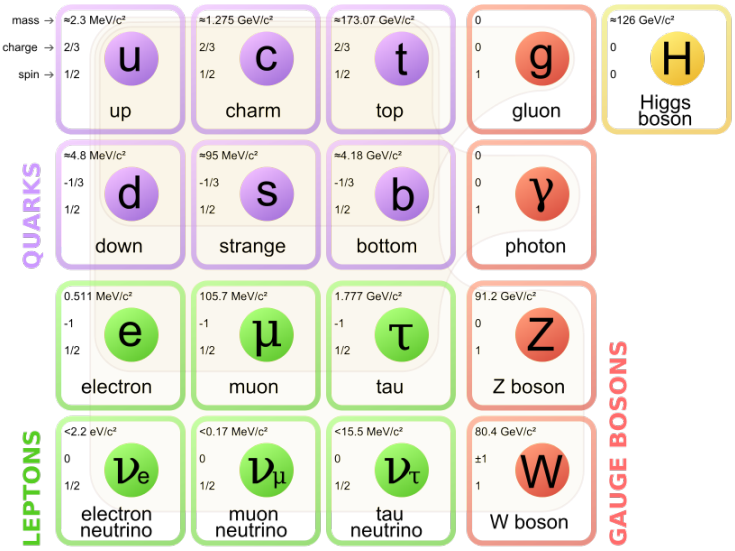

Figure 1: A schematic view of the Standard Model particles [3].

This leaves us the strong force, which is the subject of this thesis. There are in total eight gluons that, just like quarks, carry color charge. However, unlike the quarks – that carry only one color, the gluons each have one color and one anti-color. This means that gluons can couple not only to quarks, but also to each other. According to QCD theory, at normal temperature and density, quarks are not allowed to exist as free particles but must be confined within color neutral (or colorless) hadrons. The range of the strong force is therefore short and increases with increasing distance (unlike e.g. the electromagnetic force which decreases at increasing distance).

2.1.3 Quark Confinement

Quarks, under normal conditions, cannot exist freely but are bound within hadrons. This can happen in one of two ways; the quarks are either bound as a group of three quarks (antiquarks) in a baryon (antibaryon), or as a quark-antiquark pair to form a *meson*. Examples are the Λ baryon (uds) and the K^0_S meson ($d\bar{s}/s\bar{d}$), which are the particles investigated in this analysis.

The gluons act as the "glue" which holds the hadrons together. The the non-relativistic QCD potential, i.e. potential between two quarks, can be approximated to

$$V_{QCD}(r) \approx -c_F \frac{\alpha_s}{r} + kr, \tag{2.1}$$

where $c_F = 4/3$ is the color factor, α_s is the strong coupling constant, k is the string constant, and r is the distance between two quarks. At small distances the strong force potential is dominated by the first term in Eq. (2.1), thus behaving similar to the QED Coulomb potential $V_{QED} = -\frac{\alpha_{EM}}{r}$, where α_{EM} is the electromagnetic coupling constant. The strong force is, hence, weaker at small distances, so-called *asymptotic freedom*.

However, at larger distances ($r \geq 1$ fm), Eq. (2.1) is dominated by the second term, which means that the potential increases linearly with distance, while the force ($F = |dV/dr|$) remains constant [4]. As two quarks are pulled apart, a color string made up of gluons is created between them. This is described by the *Lund String Model* [7]. However, as the distance between the quarks increases so does the energy stored in the string (kr). Thus, at a certain distance it becomes more energetically favorable for the string to break and create a new quark-antiquark pair. This is displayed in Fig. 2 and illustrates why it is not possible to observe a free single quark.

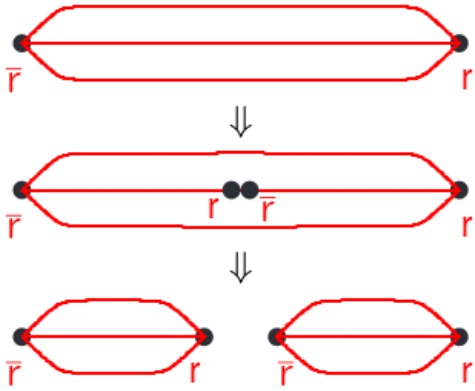

Figure 2: A gluon string between two quarks breaks to form a new quark-antiquark pair [7].

3 The Quark Gluon Plasma

By colliding two heavy nuclei, such as lead (Pb) nuclei, at relativistic energies, a medium of high temperature and density, in which colored partons (quarks and gluons) exist as free particles, can be created. In the dense medium the quarks mainly interact through the strong force and are said to be asymptotically free. This de-confined matter state is called *Quark Gluon Plasma* (QGP). Studying this in a laboratory provides the possibility to study the strong force between quarks and gluons, which is the aim of the heavy ion experiment at CERN.

As Pb nuclei collide a so-called fireball is created, which quickly expands and cools down, leading to hadronization. During the hadronization process, as the name suggests, quarks and gluons are once more bound together to form hadrons.

Figure 3 shows the QCD phase diagram where temperature is plotted against net baryon density. The diagram shows that at high temperatures and/or densities matter exists in the form of quark gluon plasma, while at lower temperatures and densities ordinary hadronic matter exists.

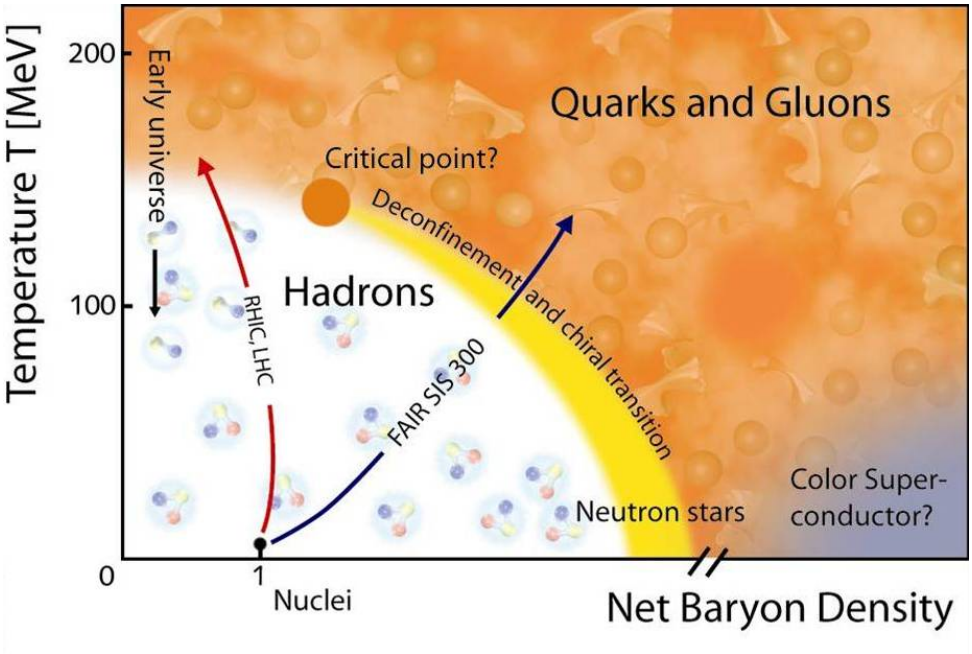

Figure 3: The QCD phase diagram with net baryon density on the x-axis and temperature on the y-axis. For low temperature and baryon density the quarks and gluons are confined within hadrons (i.e. what is referred to as "normal" hadronic matter). At high temperatures and/or high baryon densities the matter undergoes a phase transition to the QGP phase. The diagram also indicates the temperatures and densities that heavy-ion collisions at LHC and RHIC have been able to achieve. The state of the early Universe would be located in the upper left corner of the diagram. Figure from [8].

3.1 Enhancement of strange particles

Apart from the hadrons created directly from a collision, quarks in the QGP can also merge to form baryons and mesons. Especially, the threshold energy[2] for the production of a $s\bar{s}$ pair within the QGP is lower[3] than in e.g. a hadronic gas [9].

Since there is no strangeness before the collision and quarks in the QGP generally have lower transverse momentum[4], p_T, than particles created directly from the collision, one would expect to see an enhancement of strange particles at low and intermediate p_T, as compared to pp collisions where such a medium is not created. Thus, we expect to see a larger amount of strange particles in a Pb-Pb collision in the "soft" end (low p_T) of the spectrum, compared to a pp collision. Therefore, it seems a natural choice to compare the results of Pb-Pb and p-Pb collisions to pp collisions as the Pb ions are, in fact, composed of nucleons (protons and neutrons). Strangeness enhancement at low p_T is therefore seen as a sign of the formation of QGP.

[2]Threshold energy refers to the minimum energy needed for a physical process to take place.

[3]Since the quarks in the QGP are asymptotically free only the bare mass of the quarks ($m_S \approx 150$ MeV/c^2) has to be taken into account, as opposed to the constituent mass ($m_S \approx 300$ MeV/c^2) of a bound quark.

[4]Transverse momentum – momentum projection onto the plane transverse to the beam line.

3.1.1 QGP in the LHC

Comparisons between pp and Pb-Pb collisions at the LHC have shown differences such as p_T distributions, and strangeness enhancement (as mentioned above). This means that Pb-Pb collisions cannot simply be seen as a sum of proton collisions, but that other effects play a role as well. The question is whether similar effects are seen in p-Pb collisions, which is to be investigated during the course of this thesis.

3.2 Relevant concepts

3.2.1 Invariant mass

The invariant mass of a particle (e.g. a V^0) decaying into two daughter particles, in natural units ($c = 1$), is defined as follows,

$$m_{inv} = \sqrt{(E_1 + E_2)^2 - (\vec{p}_1 + \vec{p}_2)^2} \tag{3.1}$$

where $E_{1,2}$ is the daughter particle energy and $\vec{p}$ its momentum. This way, by knowing the energy and momentum of the daughter particles, one can determine the mass of the mother particle, and thus identify it.

3.2.2 Transverse momentum

The transverse momentum is defined as the momentum projection onto a plane perpendicular to the beam direction. In a coordinate system, in which the *z-axis* follows the beam direction, the transverse momentum can be defined as,

$$p_T = \sqrt{p_x^2 + p_y^2} \tag{3.2}$$

where the *x-* and *y-axis* form the plane which is perpendicular to the beam line, x being the horizontal axis. The *longitudinal* momentum p_L is defined along the *z-axis*. Before a collision the particles have a certain p_L, while $p_T = 0$. The latter is created in the collision.

3.2.3 Rapidity and pseudorapidity

Other important concepts in accelerator physics are *rapidity* (y) and *pseudorapidity* (η). The rapidity of a particle is defined as

$$y = \frac{1}{2} \ln \left(\frac{E + p_L}{E - p_L} \right) \tag{3.3}$$

where E is the energy and $p_L = p_z$ is the longitudinal momentum defined before. A particle moving in the plane transverse to the beam axis will have $p_L = 0$ which means that the rapidity, obtained from Eq. 3.3, will also be zero. For a particle moving in the +z-direction $y > 0$, while a particle travelling in $-$z-direction will have $y < 0$. Rapidity is, thus, related to the angle between the direction in which particles from the collision are emitted and the transverse plane. The difference

in rapidity of two particles is Lorentz invariant and since rapidity is related to the angular separation between the particles, also this quantity is boost invariant [10].

To determine the energy of the particle the mass needs to be known, which means that calculating y requires particle identification (PID). For high momentum particles ($p >> m$), however, the rapidity can be approximated with the pseudorapidity

$$\eta = \frac{1}{2} \ln \left(\frac{p + p_z}{p - p_z} \right) = - \ln \tan \frac{\theta}{2} \tag{3.4}$$

where the angle $\theta = 0$ is the angle between the beam pipe and the trajectory of the emitted particle.

3.2.4 Centrality and the impact parameter

The aim of this thesis is to investigate the outcome of a p-Pb collision depending on centrality. The centrality in a heavy ion collision is calculated from the following equation:

$$c(b) = \frac{1}{\sigma_{inel}} \int_0^b \frac{d\sigma}{db} db \tag{3.5}$$

where σ_{inel} is the inelastic cross section and $d\sigma/db$ is the differential cross section w.r.t the impact parameter, b [5]. With a differential cross section

$$\frac{d\sigma}{db} \approx \begin{cases} 2\pi b, b \leq b_{max} \\ 0, b > b_{max} \end{cases} \tag{3.6}$$

where b_{max} is the sum of the radii of the two colliding particles, the centrality, after integration, becomes

$$c(b) = \frac{\pi b^2}{\sigma_{inel}} \tag{3.7}$$

for $b < b_{max}$. This means that the centrality increases with increasing b, which might be considered rather counter-intuitive since a *central* collision is defined as a collision where b is small, i.e. where the overlap between the particles is large, while in a *peripheral* the overlap is small, hence a large b (see Fig. 4).

The centrality of a collision is estimated through measurements of the charged particle multiplicity measured by the ALICE V0 detector.

3.2.5 The Nuclear modification factor R_{CP}

In a central collision most of the nucleons will participate, while in a peripheral collision only a small fraction of nucleons are involved. One might therefore expect peripheral heavy ion collisions to show features similar to those of proton-proton collisions (where only the two colliding protons are involved). Comparing the p_T spectrum of a central collision to that of a peripheral collision could therefore provide an insight into how the creation of QGP is affected by the number of participating nucleons. A way to examine the centrality dependence of a p-Pb collision is to

[5] The impact parameter b is defined as the distance, in the transverse plane, between the centers of the two colliding particles.

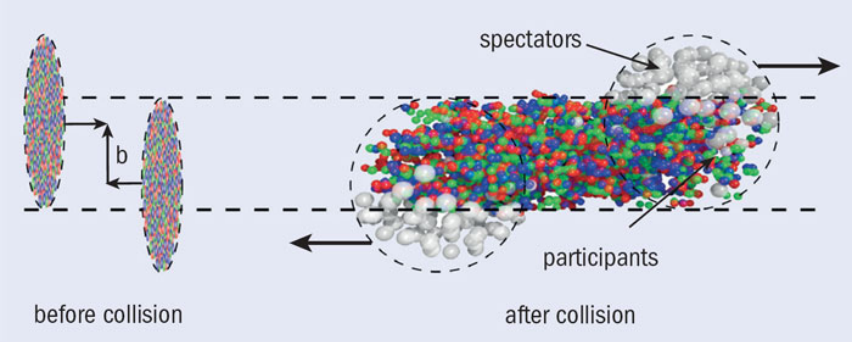

Figure 4: The relationship between the number of participants (i.e. nucleons participating in a collision) and the impact parameter b in a Pb-Pb collision. Figure from [11].

calculate the *central-to-peripheral nuclear modification factor*, R_{CP}, which describes the ratio between the number of central and peripheral collisions. This ratio, as a function of p_T, is defined as

$$R_{CP} = \frac{\langle N_{coll} \rangle_P}{\langle N_{coll} \rangle_C} \times \frac{d^2 N_{pA}^C / dp_T dy}{d^2 N_{pA}^P / dp_T dy} = \frac{\langle N_{coll} \rangle_P}{\langle N_{coll} \rangle_C} \times \frac{yield_{pA}^C(p_T)}{yield_{pA}^P(p_T)} \tag{3.8}$$

where N_{coll} is the number of binary nucleon-nucleon collisions for a certain centrality bin. N_{coll} cannot be measured directly from a collision, so it has to be calculated using the *Glauber model*. For a more extensive discussion on this, see [12].

3.2.6 Radial flow

As two ions collide to create QGP, the nuclear matter is first highly compressed into a fireball and heated (as mentioned in Sec. 3). This gives rise to a pressure gradient from the dense center to the edge of the medium. For central heavy ion collisions this pressure gradient is radially symmetric which, as the QGP cools and expands, leads a flow of particles – particles moving in a collective motion – radially outwards, called *radial flow*. Thus, particles in the expanding medium do not only experience thermal motion, but also get a radial velocity component, which leads to an increase in particle momentum. The momentum of a particle is proportional to the particle mass ($p = \gamma m v$), so when hadrons are formed the hadrons with higher mass get a higher momentum than the hadrons with lower mass, which means that the effect of radial flow is larger for heavier particles [13]. A graphical description of flow is given in Fig. 5.

Signs of radial flow can be seen in Fig. 6, where the spectra of $\pi^{\pm}$, $K^{\pm}$ and $p + \bar{p}$ from central Pb-Pb collisions are compared to those from pp collisions. At low p_T there is a higher abundance of lighter hadrons ($\pi^{\pm}$) compared to heavier hadrons ($p, \bar{p}$), which for Pb-Pb are instead rather depleted when comparing to pp collisions. Moving to higher p_T, however, there is a clear boost in the p_T spectra from Pb-Pb collisions. This enhancement is more pronounced for the heavier hadrons, which is consistent with the effects of radial flow.

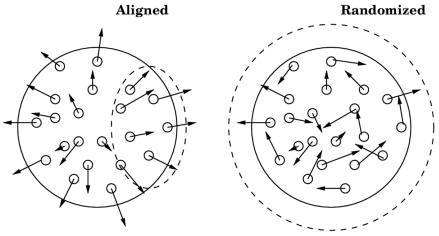

Figure 5: Figure showing the concept of flow in a heavy ion collision.

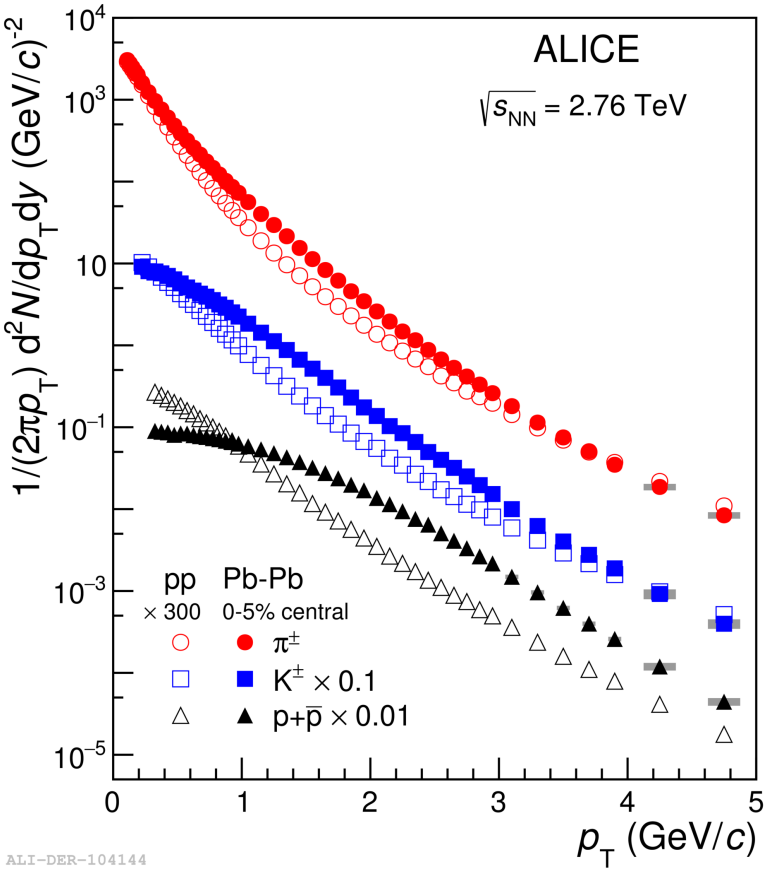

Figure 6: Pion, kaon and proton spectra in p+p and Pb+Pb collisions at $\sqrt{s_{NN}}$ = 2.76 TeV. The p+p spectra are scaled for a better comparison of the shapes. Figure and caption from [14].

3.2.7 Λ/K^0_S – the particle yield ratio

The effects of flow also appear when studying the ratio of Λ/K^0_S, i.e. the baryon-to-meson ratio. At low p_T ($p_T < 2$ GeV/c) mainly thermal effects are observed and the yield ratios are similar for the most central and the most peripheral collisions. Studies of QGP in heavy ion collisions indicate that the medium behaves almost like a perfect fluid (i.e. small shear viscosity relative to the entropy density). Hence, the steep increase in this part of the spectrum is quite well understood and qualitatively described by hydrodynamics. At high p_T what is observed is predominantly the effects of fragmentation (i.e. jets). This is not affected by collective effects, which

explains the flattening of the spectrum in the high p_T range.

These parts of the p_T spectrum are consistent for pp, p-Pb and Pb-Pb collisions. However, at intermediate p_T the spectra from the different types of collisions show a discrepancy. In Pb-Pb collisions an enhancement in the Λ/K^0_S ratio has been observed in the mid-p_T region, a feature which, seen in Fig. 7, increases with centrality. As seen in the figure this effect is not very pronounced in pp collisions, where the spectrum does not change much with respect to the initial energy of the collision. The height of the maxima of the most central and peripheral Pb-Pb collisions differs by almost a factor of three. The fact that the maxima for the different centralities are slightly shifted towards higher p_T is another indication of an increasing radial flow for more central collisions, as the particles get more boosted toward higher momenta. Another thing to note is that the spectrum of the most peripheral Pb-Pb collisions agrees very well with that of the pp collisions, indicating that similar processes are taking place in the two cases.

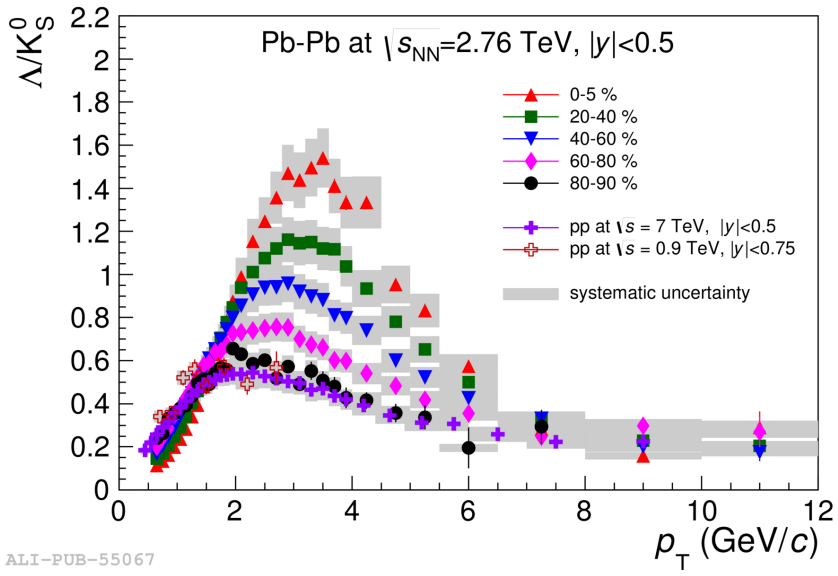

Figure 7: Λ/K^0_S ratios as a function of p_T for different event centrality intervals in Pb-Pb collisions at $\sqrt{s_{NN}} = 2.76$ TeV and pp collisions at $\sqrt{s} = 0.9$ and 7 TeV. Figure and caption from [16].

The reason for the apparent p_T enhancement seen in the Λ/K^0_S ratio, at intermediate p_T, is so far not fully established. Suggestions, as discussed in [2] include a combination of effects such as *quark recombination*, which is a hadronization mechanism that allows two or three quarks to coalesce and form a meson or a baryon. Just as in the case of flow, the hadrons consisting of three quarks (baryons) will have a higher p_T than the hadrons made out of two quarks (mesons), provided that the initial quarks had similar p_T. This model, however, overestimates the ratio in the p_T region $2-5$ GeV/c, hinting that additional processes involved. Models trying to describe these processes, such as the EPOS model [17], attempt to bridge the gap between soft and hard processes.

4 The ALICE Experiment

The name ALICE is an acronym for A Large Ion Collider Experiment. As the name reveals, the 26 m long, 16 m tall, and 16 m wide ALICE detector, with a weight of approximately 10,000 tons, is constructed to study the strong force through collisions of heavy ions. For particle identification (PID), ALICE measures the particle momentum p, energy loss dE/dx, time of flight (TOF), as well as transition radiation and Cherenkov radiation.

4.1 The Detectors

To obtain information about a collision, one needs to measure the remnant particles created from the colliding nuclei. To identify the different particles (protons, pions, electrons...) a set of detectors is required, which all measure different aspects of the collision. These 15 sub-systems are built in layers around the collision to provide efficient tracking and PID. The tracking system consists of cylindrical detectors surrounded by a magnetic solenoid. The solenoid serves to produce a magnetic field which bends the tracks of the charged particles, so that the charge and momentum can be determined. Below a brief introduction on the different detectors is given, starting from the center and moving outwards. A schematic view of the detector is shown in Fig. 8.

4.1.1 Tracking the particles

The tracking system of the ALICE detector is located in the central barrel and is divided into two sub-detectors; the *Inner Tracking System* and the *Time Projection Chamber*.

ITS – Inner Tracking System
The first and innermost detector surrounding the interaction point is the Inner Tracking System. This detector is divided into three sub-detectors – the *Silicon Pixel Detector* (SPD), *Silicon Drift Detector* (SDD), and *Silicon Strip Detector* (SSD) – each constructed in two layers. The task of the ITS is to locate the primary and secondary vertices with sub-milimeter precision.

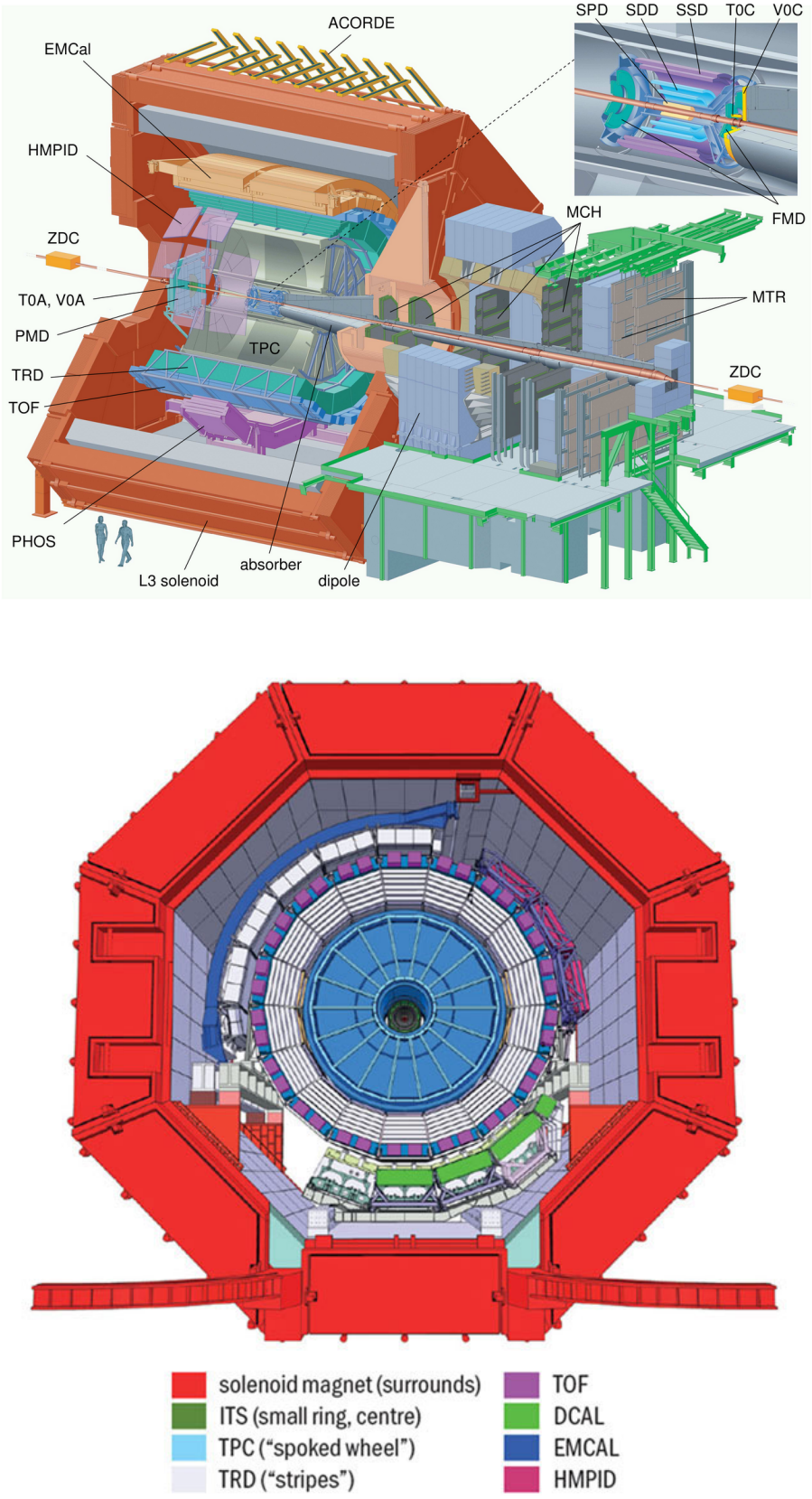

Figure 8: (a) Schematic of the ALICE detector [23] showing the various subdetectors, together with a cross-sectional view (b) [24].

TPC – Time Projection Chamber
The main ALICE tracking detector is the TPC, which, due to its geometrical acceptance[6], is able to provide information on thousands of charged particles in a single collision. This detector is constructed as a cylinder filled with gas (a mixture of Ne-CO_2-N_2), with an electrode at the center separating the cylinder into two halves. As the charged particles pass through the gas they leave behind tracks of ionized particles. A strong electric field ($\sim$ 400 V/cm) makes the liberated electrons drift towards the end plates of the detector, where the signal is amplified and recorded in Multi-Wire Proportional Chambers (MWPCs). As the electrons approach the anode wires, the electric field around the wires causes the electrons to accelerate and further ionize the gas. This gives rise to an avalanche of positive ions, which induce a current on the pads (electrodes) in the cathode plane of the MWPCs. A two-dimensional position of a track is obtained by measuring the coordinates where the drift electrons hit the pads. The third dimension – the distance of the track from the end plate – is attained by measuring the drift time of the electrons, i.e. the time it takes for the electrons to reach the anode wires. This measurement is done for up to 159 space points along each track, providing reliable reconstruction of the tracks of the many particles created in a heavy ion collision [18, 19].

4.1.2 Particle Identification

An important feature of the ALICE detector is the PID, to which several subdetectors are dedicated; the *Time-of-Flight* system (TOF), the *High Momentum Particle Identifier Detector* (HMPID), and the *Transition Radiation Detector* (TRD). Also the energy loss dE/dx measured in the ITS and TPC is used for PID.

TRD – Transition Radiation Detector
Located outside the TPC is the Transition Radiation Detector, consisting of 18 modules. Each module contains MWPCs that are filled with $XeCO_2$ gas. As a charged particle passes the boundary of two media with different refraction indices[7], radiation is emitted in the form of X-ray photons [20]. This *transition radiation* is then amplified and detected in the MWPCs. The TRD is used to distinguish between electrons and pions above 1 GeV/c and is also used to trigger on electrons and high-energy particles in jets [21].

TOF – Time of Flight
The task of the TOF is to differentiate between pions, kaons, and protons, by measuring the time it takes for a particle to travel from the collision interaction point to the detector. The TOF system consists of a cylindrical shell made up of 18 sectors – each of which is divided into 5 modules. The modules consist of Multigap Resistive Plate Chamber strips (MRPCs), with an anode pickup electrode at the center and cathode pickup electrodes at each side (see Fig. 9).

As a charged particle passes through the gas in the MRPC gaps it ionizes the gas which, due to a high electric field, starts an electron avalanche. The avalanche

[6]The TPC covers 2π in azimuthal angle and $|\eta| < 0.9$ in pseudorapidity (polar angle).
[7]In this case the electrons pass through a radiator positioned in front of the drift chamber.

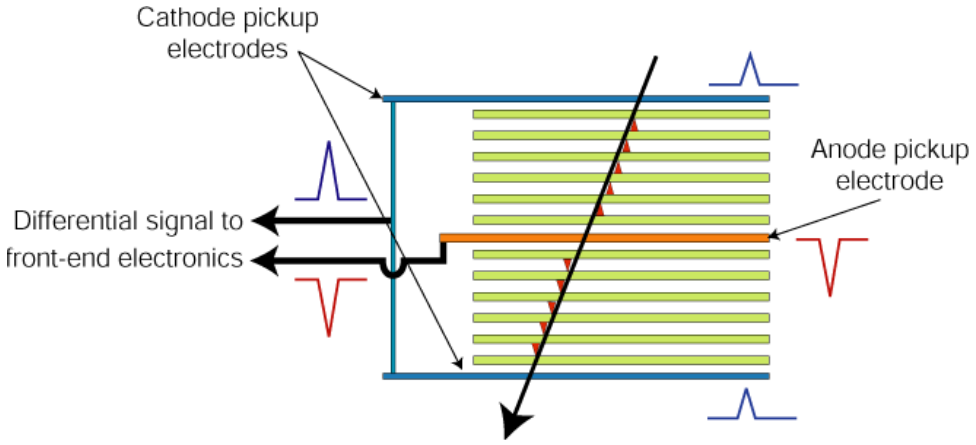

Figure 9: The layout of a MRPC [22].

in each gap is stopped by the resistive plates, but induces a signal on the electrodes which corresponds to the time-of-flight difference for particles of similar momentum but different mass. The total signal is then the sum of the signals from all gaps in the MRPC [22].

HMPID – High Momentum Particle Identifier Detector
A charged particle traveling through a dielectric medium (e.g. a liquid), at a speed that is higher than the phase velocity of light in that medium, polarizes the medium along its path and gives rise to the emission of *Cherenkov radiation*. The Cherenkov radiation is emitted in the shape of a cone (like a shockwave) with an angle that depends on the velocity of the propagating particle. The photons are detected by a photon counter, which consists of a photo-electrode with a thin layer of CsI[8]. So, by measuring the angle of the emitted radiation, the velocity of the particle can be determined and since the momentum is known from the TPC, the mass can be deduced and the type of particle determined.

EMCal – The Electromagnetic Calorimeter
The EMCal is a Pb-scintillator sampling calorimeter that measures the energy deposited, mainly, by photons and neutral hadrons, which are not seen by the inner detectors. It consists of several alternating layers of lead and scintillators. A charged particle sets off an electromagnetic shower in the lead layers and the resulting photons are absorbed in the scintillator. The radiation from the scintillator is then collected by optical fiber cables. Since electrons leave most of their energy in the calorimeter while hadrons do not, this detector is also useful for the discrimination of electrons from hadrons [25].

PHOS – The Photon Spectrometer
In addition to the EMCal, there is another electromagnetic calorimeter; namely the Photon Spectrometer. This high-resolution calorimeter measures photons and neu-

[8]As a photon hits the CsI surface, there is a $\sim 25\%$ probabilty of producing an electron, which in turn can be detected.

tral mesons over a smaller area of the detector but with better precision than the EMCal [26]. In order to learn the temperature of the QGP created in heavy-ion collisions, it is important to measure thermal photons emitted by the medium. PHOS consists of detection channels of dense scintillator lead-tungsten crystals divided into 4 modules, where each crystal is connected to an Avalanche Photo Diode (APD) and a Charge Sensitive Preamplifier (CSP) [27].

4.1.3 Forward and Trigger Detectors

Apart from the above mentioned detectors a set of smaller specialized detector systems, mainly for triggering purposes and multiplicity determination, are located at forward rapidity close to the beam line. The T0 detector, consisting of two sets of Cherenkov counters (T0A and T0C), is used as a trigger and timing detector which measures the collision time with very high precision. It is also used to measure the start time of the TOF, which is needed for accurate PID. The V0 is a scintillator detector that provides minimum bias triggers for the central barrel detectors and, along with the Forward Multiplicity Detector, FMD ($-3.4 < \eta < -1.7$, $1.7 < \eta < 5.0$), provides information on charged-particle multiplicity distributions [28]. The multiplicity and spatial distribution of photons from each collision is measured by the Photon Multiplicity Detector, PMD. The Zero Degree Calorimeter, ZDC, is used to measure the energy of spectator nucleons in a collision (nucleons that did not participate) in order to determine the overlap between two colliding nuclei, which is directly related to the centrality of a collision [29]. The final trigger detector in ALICE is the so called ALICE COsmic Ray Detector, or ACORDE, which is used as a cosmic ray trigger. This is useful for calibrations when there is no beam in the LHC. It also detects atmospheric muons, allowing for the study of cosmic rays [30].

4.1.4 Muon Spectrometer

Another forward detector is the Muon Spectrometer, which consists of a dipole magnet and tracking and trigger chambers. The tracking chambers provide a two-dimensional location of the muons and the trigger chambers work as triggers on muon pairs produced from heavy particle decays. An absorber is placed in front of the spectrometer in order to separate muons from hadrons that were produced in a collision (the hadrons are absorbed while muons pass through almost unaffected) [18].

4.1.5 Detectors involved in this analysis

The main detectors used in this analysis are the ITS and the TPC for PID, as well as the V0 for centrality estimation.

5 Analysis on K^0_S and Λ spectra

The analysis in this thesis has been aimed to examine the p_T spectra of the K^0_S and Λ particles, created in p-Pb collisions, in order to investigate the central-to-peripheral nuclear modification factors of the two particles and finally the Λ/K^0_S ratio for different collision centralities. Examining the particle yield ratios in this way provides an insight into the properties of the created medium.

5.1 V^0 track reconstruction

After a neutral V^0 particle is created in the collision it will decay into two charged daughter particles. The topology of these decays is that of a V shape, hence the name V^0 (see Fig. 10). The K^0_S will most likely decay weakly into a π^+ and a π^- and Λ into a π^- and a proton (p). Since these daughter particles are electromagnetically charged they leave tracks in the detector and by reconstructing the tracks back to the secondary vertex (where the V^0 decays), the V^0 particle can be identified. The secondary vertex is reconstructed using a V^0 finder algorithm, that can be either online (operating during the track finding) or offline(executed after the track finding algorithm). In this analysis the offline V^0 finder is used. To make sure that the reconstructed V^0's are the ones created in the initial vertex some selected cuts are applied to the raw data. These cuts are discussed in more detail in Sec. 5.2.

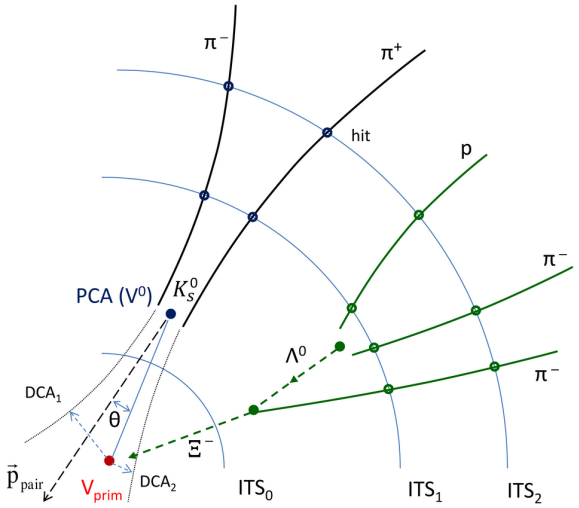

Figure 10: V^0 decay topology. The primary vertex here is denoted as V_{prim}. DCA_1 and DCA_2 are the distances of closest approach between the primary vertex and the extended charged particle tracks (referred to in this thesis as $DCA_{d^{\pm}-PV}$). The point of closest approach between the daughter particle tracks, PCA, is located about the second vertex. The distance between the daughter particles, at this point, will hereinafter be referred to as DCA_{d-d}. The image also shows secondary Λ's from the Ξ^- decay. The solid lines represent reconstructed particle tracks from detected particles, which are used to extrapolate the secondary vertex V^0 candidate. Figure taken from [23].

In order to establish what kind of V^0 particle that has been detected, i.e. whether

it is a Λ or a K^0_S, the mass of the particle needs to be determined. To calculate the mass the momentum and the energy of the V^0 need to be known. The three-dimensional momentum vector is calculated from the known momentum vectors of the daughter particles according to:

$$p_{i,V^0} = p_{i,1} + p_{i,2} \tag{5.1}$$

where $p_{i,1}$ and $p_{i,2}$ are the momenta of the daughter particles and $i = x, y, z$. Assuming the masses of the daughter particles it is possible to calculate their energy using Eq. 3.1. Once the 4-momenta of the daughter particles are known, the energy of the of the V^0 can be calculated as

$$E_{V^0} = E_1 + E_2 \tag{5.2}$$

and thus also the invariant mass, using Eq. 3.1.

5.2 Cuts

To make sure that our V^0 candidates are indeed created at the primary vertex and to assure full TPC acceptance, a number of cuts were added to help "clean up" the MC data. The cuts are listed in Table 1.

Decay radius (r_{dec}): In order to be able to separate the secondary vertex from the primary vertex a cut is added to the decay radius, which ensures that all V^0 candidates within 5 cm from the primary vertex are excluded from the analysis. r_{dec} is shown in Fig. 11.

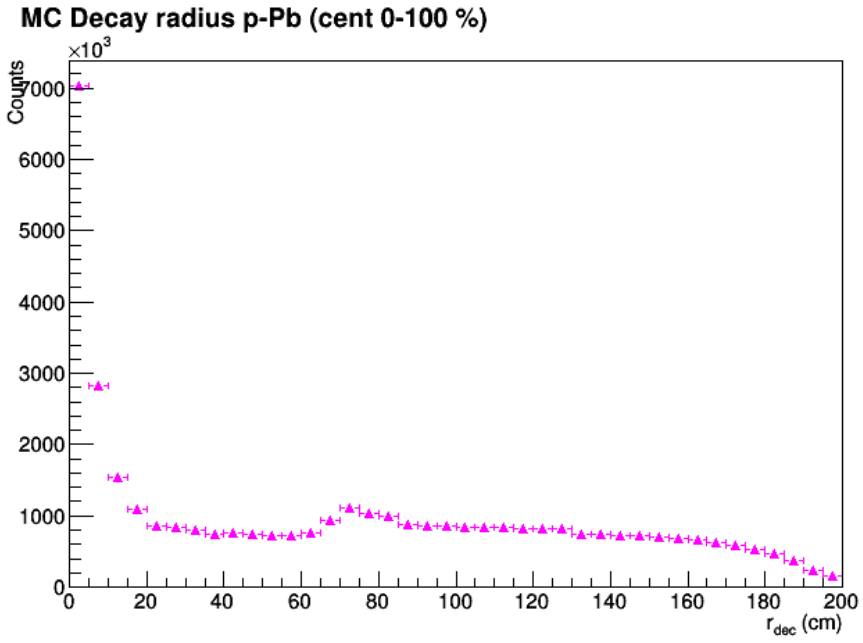

Figure 11: MC Decay radius, r_{dec}.

DCA$_{\mathbf{d^{\pm}-PV}}$: A cut is also added to the DCA – distance of closest approach – between the daughter particles and the primary vertex (see Fig. 12). Putting

a minimal limit on the DCA will ensure that the daughter particle tracks are not mixed up with any particles coming from the primary vertex.

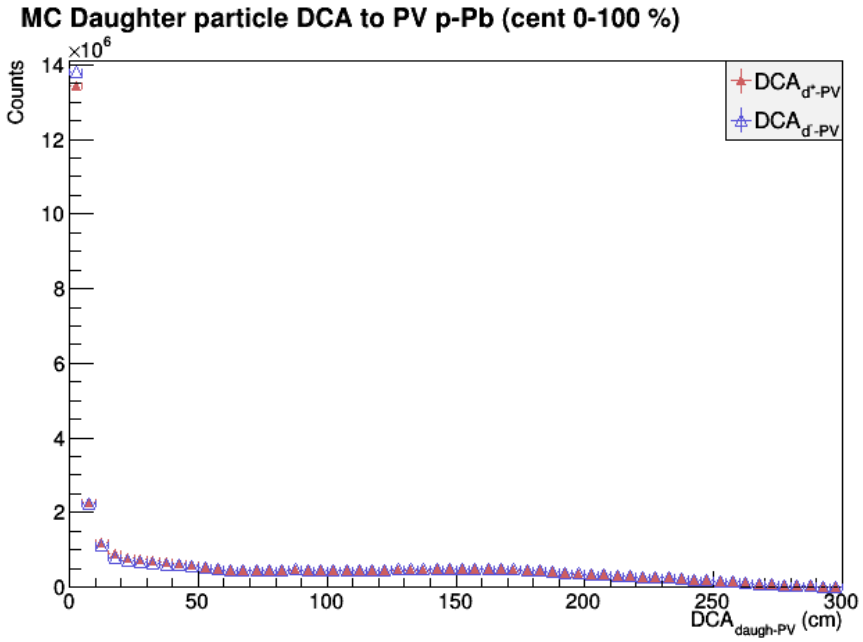

Figure 12: MC DCA between the charged daughter particles and the PV.

$\mathbf{DCA_{d-d}}$: To assure that the daughter particles both come from the same secondary vertex, an upper limit is applied to the DCA of the daughter particles. The DCA distribution of the daughter particles is shown in Fig. 13.

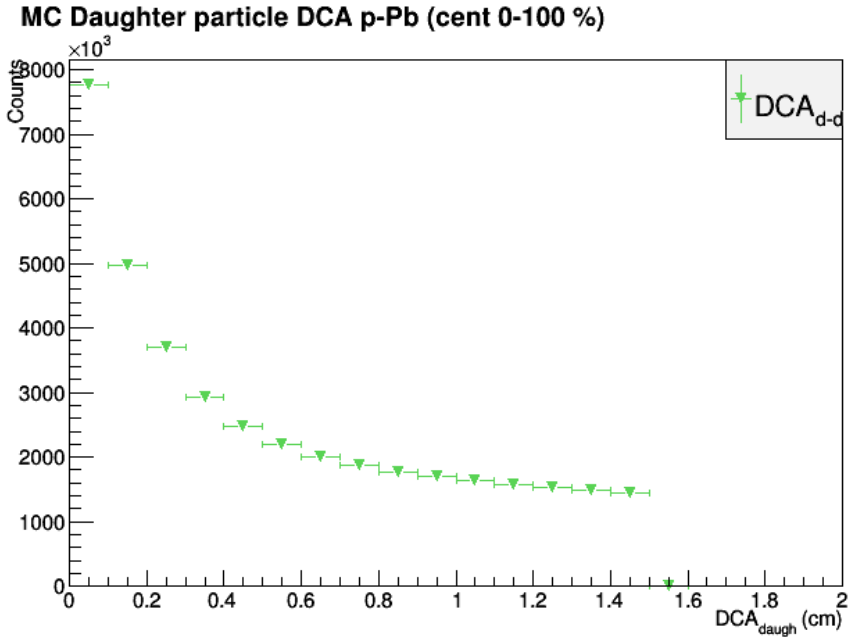

Figure 13: MC DCA between the daughter particles.

Pseudorapidity (η): A cut is applied on the pseudorapidity in order to include

tracks only within full the TPC acceptance. Any tracks outside the pseudorapidity range $|\eta| < 0.8$ might risk not getting fully projected in the TPC, leading to reduced detector efficiency. This is done for both the V^0 mother particle and the charged daughter particles [19]. The pseudorapidity distributions of the V^0 particles and the daughter particles are presented in Fig. 14.

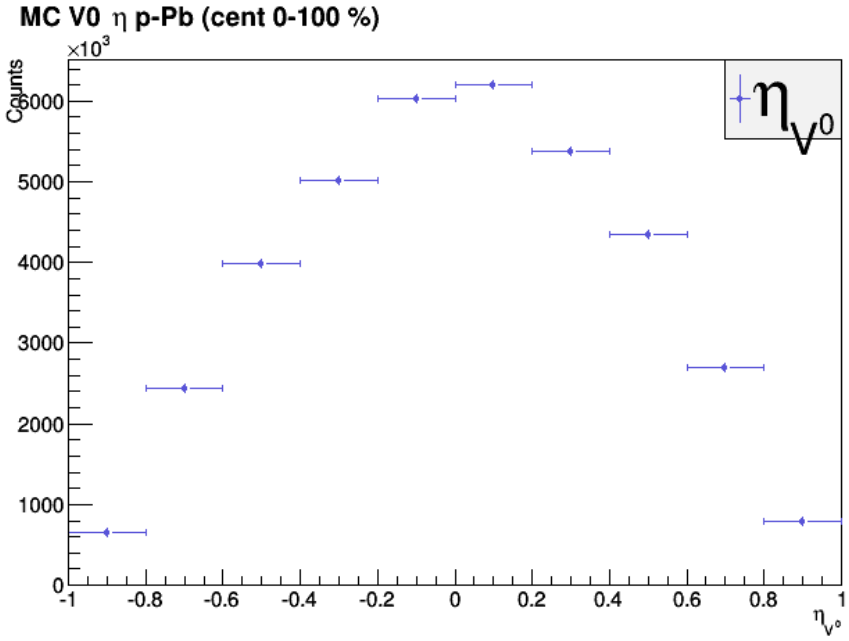

(a) V^0 particle pseudorapidity, η_{V^0}.

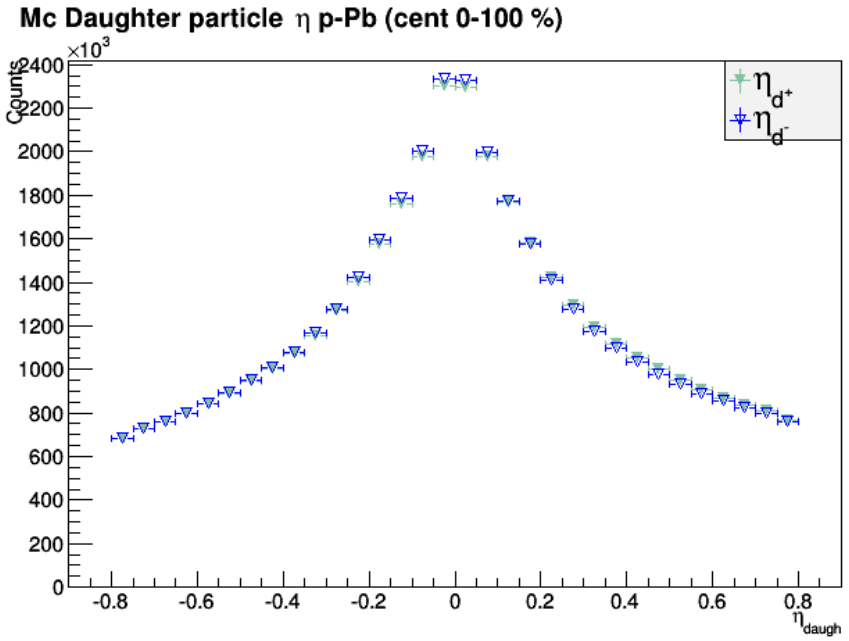

(b) Daughter particle pseudorapidity, η_{daugh}.

Figure 14: MC Pseudorapidity, η.

p_T cut: A cut is also applied to the transverse momentum at $p_T = 0.4$ GeV/c.

This is due to the high amount of background at low p_T, which makes it difficult to separate signal from background.

A summary of the cuts that are used in the analysis is given in Table 1.

Table 1: V^0 candidate cuts.

Variable	**Cut**
r_{dec}	$5 - 100$ cm
$\mathrm{DCA}_{d^{\pm}-PV}$	> 0.1 cm
DCA_{d-d}	< 1 cm
$\lvert\eta_{V^0}\rvert$	< 0.8
$\lvert\eta_{daugh}\rvert$	< 0.8
p_T	> 0.4 GeV/c

5.3 Monte-Carlo p-Pb study

In order to properly analyze data obtained from real collisions, a good way to start out is by working with Monte-Carlo (MC) *simulated data*, since this provides a possibility to test if one's analysis is robust and reliable. A MC event generator is used to recreate the outcome expected from a real collision, but where the properties of the particles – such as momentum, mass, charge, and decay products – are already known. A detector simulation, called GEANT, is included in order to reproduce the, so called, *raw data* that is obtained from real collisions, after which the MC data undergoes the same analysis as the real data, but also allows detector efficiencies, feeddown etc. to be estimated and corrected for. The different types of MC data used in the MC analysis are listed:

- MC_{gen} – The generated MC data in this thesis, before the detector simulation has been added, for which all the particle properties are known.
- MC_{truth} – After the generated data has been "propagated" through the detector, but still carry PID label (particle properties are still known).
- MC_{blind} – The MC equivalent of *real data*, i.e. where no PID label is used.

5.4 Corrections

Using MC data, where the all properties of a particle is known, correction factors for inaccuracies such as feeddown and detector acceptance and efficiency can be calculated.

5.4.1 Feeddown

Although the Λ spectrum mainly consists of particles created in the initial collision (so called primary particles), part of the contribution comes from particle decays. These secondary Λ's are created primarily from Ξ^0 and Ξ^- decays, with some minor contributions from Ω decays.

In order to get a clean spectrum it is necessary to correct for this *feeddown* of particles. Since there is no significant contribution of secondary decays into K^0_S, this effect mainly concerns the Λ particle. The feeddown correction is done by first estimating the number of secondary Λ particles. Using a generated MC PID label, a two-dimensional response matrix, which correlates the p_T spectrum of the detected Λ particles with that of the Ξ decay, can be constructed [31]. A feeddown correction is carried out for the p_T spectrum by removing the secondary particle contribution from the spectrum. The Λ feeddown distribution is shown in Fig. 15.

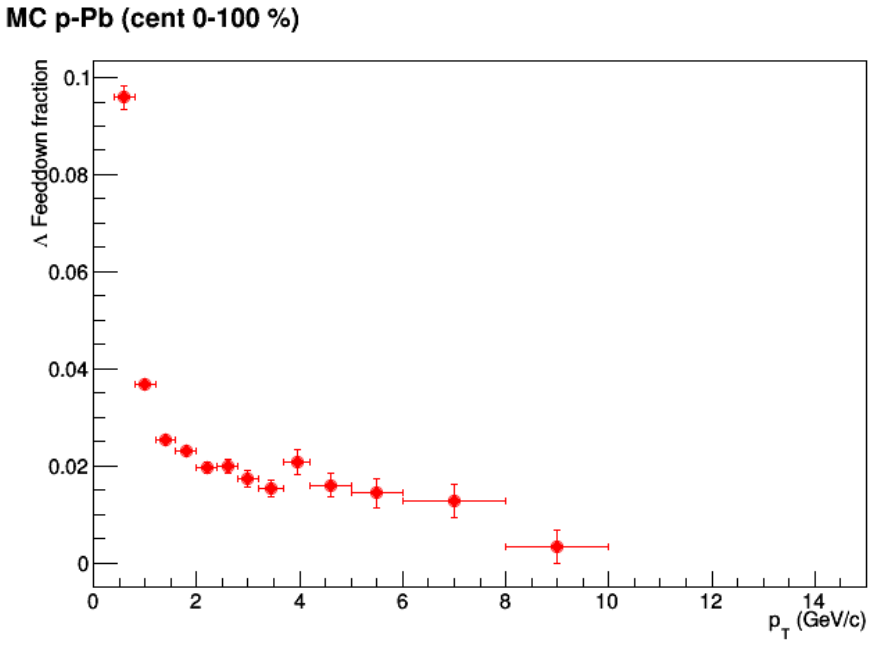

Figure 15: Λ contamination from Ξ decays as a function of p_T.

5.4.2 Acceptance × Efficiency

Since the detector does not detect all of the V^0 particles created in a collision, an efficiency correction has to be made to correct for any shortcomings in the detector performance as well as track reconstruction and selection deficiencies. By efficiency, here, is meant the detector efficiency × detector acceptance and is defined as the ratio between the reconstructed primary MC particles, here called MC_{rec}, and the number of "true" particles at generator level, MC_{gen}. The efficiency calculated for the two particles, after all cuts have been done, is displayed in Fig. 16. The efficiency for different centralities is presented in Fig. 17. Comparing these to the minimum bias efficiency in Fig. 16 shows that the efficiency is roughly the same for different centralities.

An efficiency correction is carried out by multiplying the uncorrected raw K^0_S and Λ spectra (MC_{blind} for the MC analysis) by the efficiency correction factor 1/efficiency.

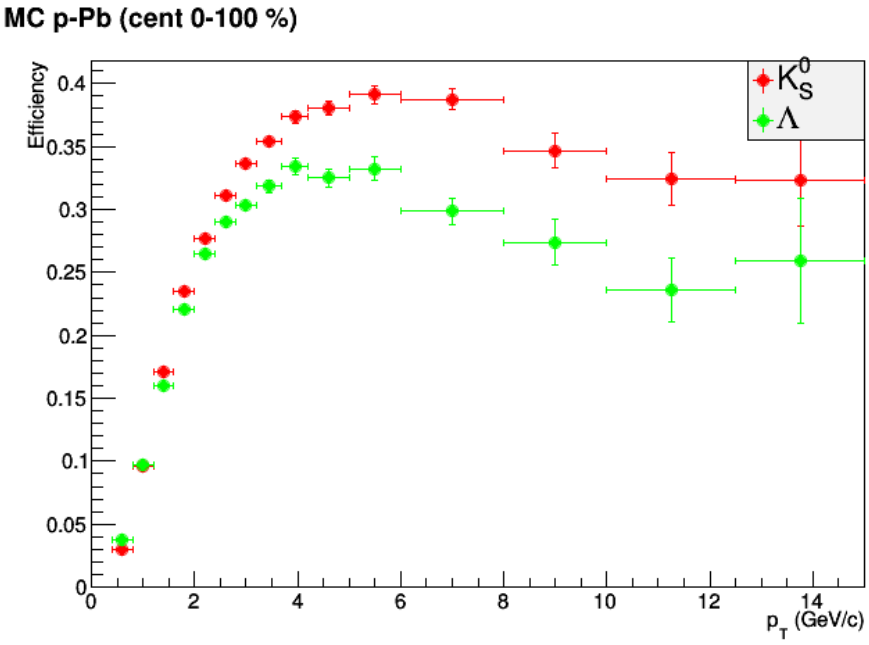

Figure 16: Efficiency for minimum bias K0 and Λ, with cuts.

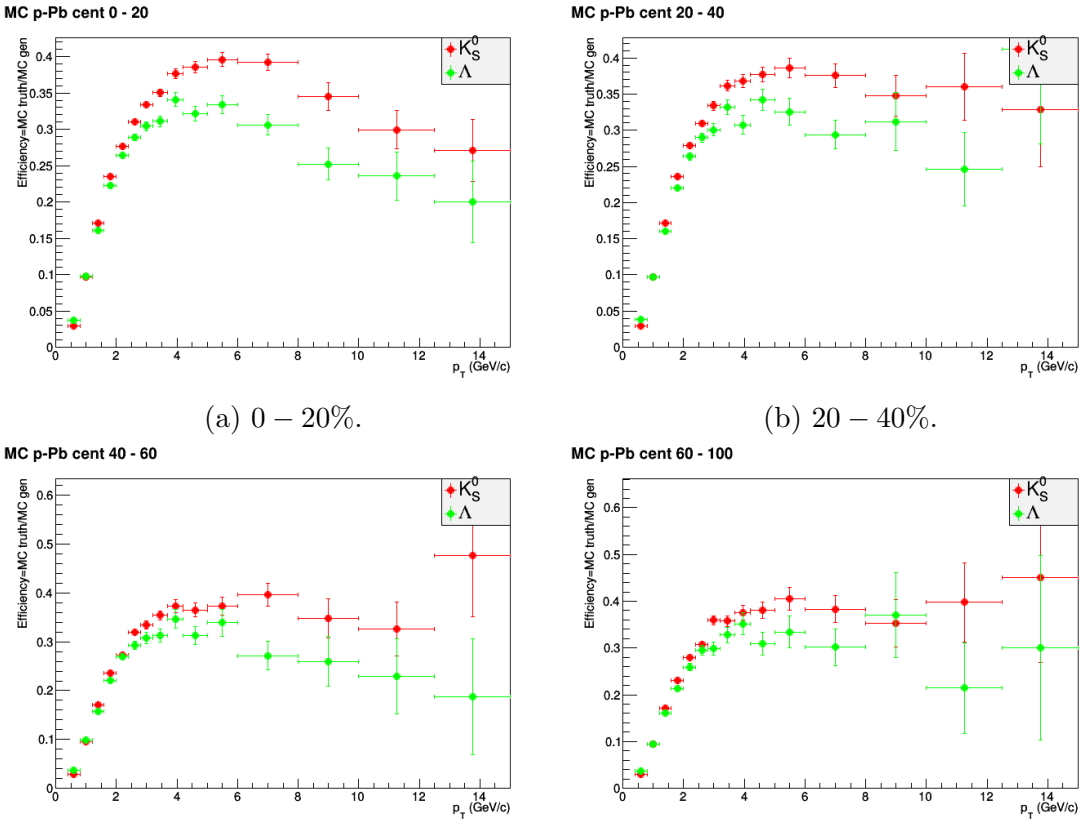

(a) $0 - 20\%$.

(b) $20 - 40\%$.

(c) $40 - 60\%$.

(d) $60 - 100\%$.

Figure 17: Efficiency for different centrality bins for K^0_S and Λ.

5.5 The Invariant Mass Distribution

The foundation of this analysis is a two-dimensional spectrum with the invariant mass difference Δm, along the y-axis, and the transverse momentum p_T, along the x-axis, of each particle. This can be seen, with the selected cuts, for the K_S^0 and Λ in Fig. 18. The framework used in the analysis is ROOT [32], which is used to sort large amounts of data into a data tree, provided by the ALICE collaboration, that contains all available information about the V^0 particles. In the tree the Δm of the K_S^0 and Λ particles is defined as

$$\begin{aligned} \Delta m_{K_S^0} &= m_{V^0} - m_{K_S^0}^{PDG} \\ \Delta m_{\Lambda} &= m_{V^0} - m_{\Lambda}^{PDG} \end{aligned} \tag{5.3}$$

where m_{V^0} is the mass assumed for the V^0 depending on its decay products ($\pi^+ + \pi^-$ for K_S^0 and $p + \pi^-$ for Λ).

From the two-dimensional spectrum the Δm of the particle, for different p_T bins, can be investigated. In order to know if the method – and hence the results – is reliable, the first thing to do is to check whether the simulated MC_{blind} agrees with MC_{truth}, since MC_{blind} here is a similar data set as the data obtained from real collisions. The same cuts that are made on MC_{blind} will hence also be made on the data.

Figure 18 shows the Δm vs p_T distributions for K_S^0 and Λ. A cut was added to include only V^0's with $p_T > 0.4$ GeV/c, since the background below this part of the p_T spectrum was too high to properly distinguish the peak (an effect more expressed in Λ's) . The p_T bins are chosen so that the bin size increases with increasing p_T, due to decreasing statistics, while the Δm bins are kept constant. The Δm distribution is analyzed for each p_T bin, from which the signal (the number of V^0s) can be extracted.

In order to obtain the correct number of V^0 particles, the background has to be extracted from the Δm spectrum, so that only the signal itself remains. This is done as described in Sec. 5.5.1.

Figures 19 and 20 show the Δm distributions of the K_S^0 and Λ particles for three different p_T bins; $0.4 < p_T < 0.8$ GeV/c (low p_T), $3.7 < p_T < 4.2$ GeV/c (mid-p_T) and $8.0 < p_T < 10.0$ GeV/c (high p_T). One may notice that the background decreases further up in the p_T spectrum, but that is also true for the amount of signal particles in the peak.

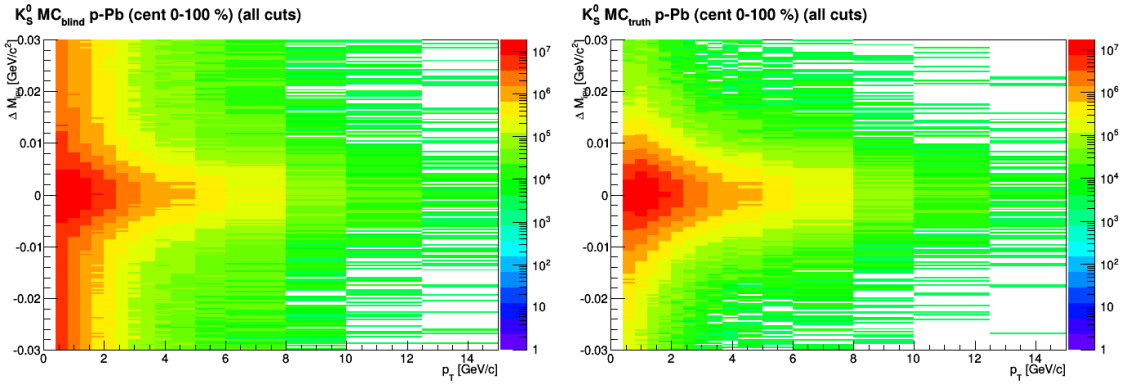

(a) MC$_{blind}$ $\Delta m_{K^0_S}$ vs p$_T$.

(b) MC$_{truth}$ $\Delta m_{K^0_S}$ vs p$_T$.

(c) MC$_{blind}$ Δm_{Λ} vs p$_T$.

(d) MC$_{truth}$ Δm_{Λ} vs p$_T$.

Figure 18: Δm vs p_T for the K^0_S meson and Λ baryon. The figures on the left show the MC$_{blind}$ spectra, while the figures on the right show the MC$_{truth}$ spectra. A cut to select $p_T > 0.4$ GeV/c, to avoid the background in the low p_T region, has been added.

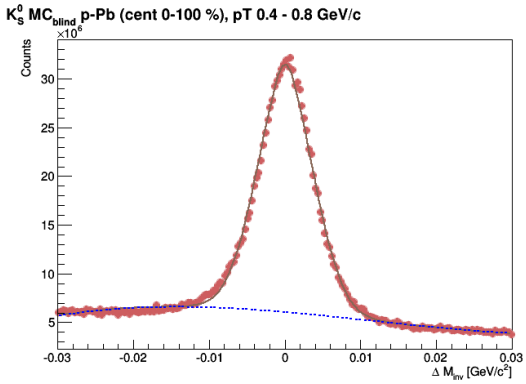

(a) MC$_{blind}$ $\Delta m_{K^0_S}$, low p_T.

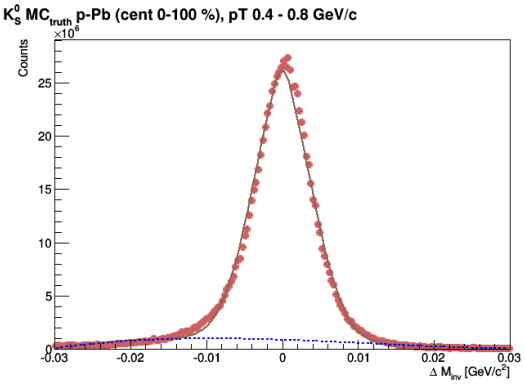

(b) MC$_{truth}$ $\Delta m_{K^0_S}$, low p_T.

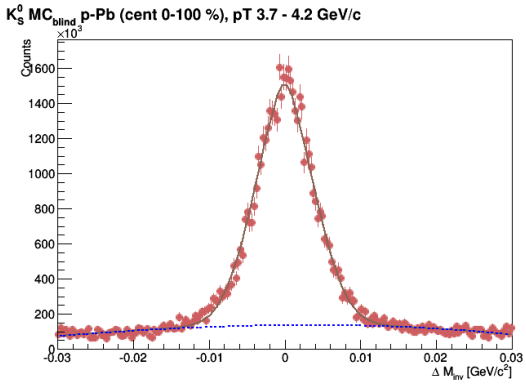

(c) MC$_{blind}$ $\Delta m_{K^0_S}$, intermediate p_T.

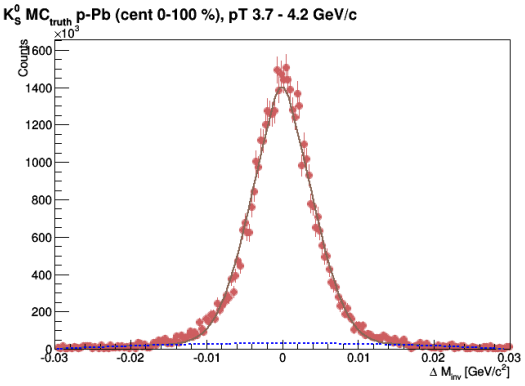

(d) MC$_{truth}$ $\Delta m_{K^0_S}$, intermediate p_T.

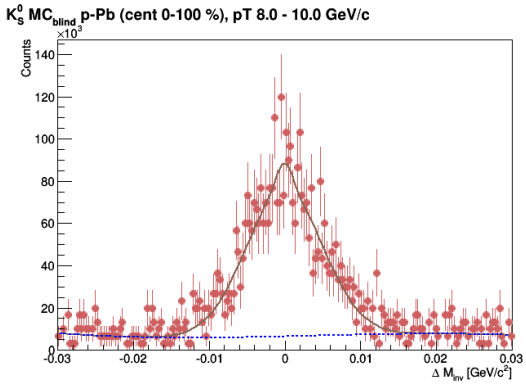

(e) MC$_{blind}$ $\Delta m_{K^0_S}$, high p_T.

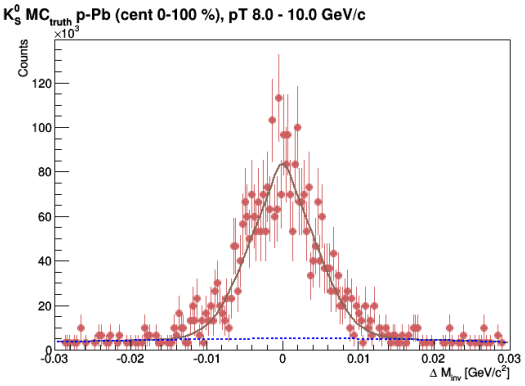

(f) MC$_{truth}$ $\Delta m_{K^0_S}$, high p_T.

Figure 19: The MC$_{blind}$ (left) and MC$_{truth}$ (right) Δm for low ($0.4 < p_T < 0.8$ GeV/c), intermediate ($3.7 < p_T < 4.2$ GeV/c) and high ($8.0 < p_T < 10.0$ GeV/c) p_T.

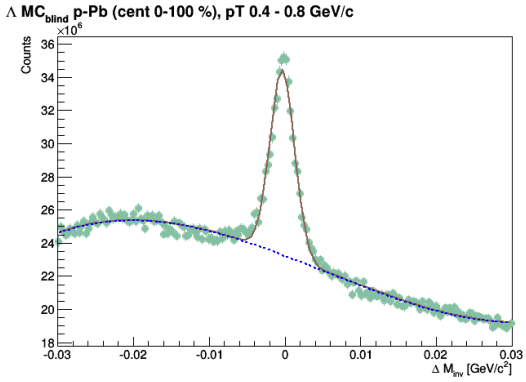

(a) MC_{blind} Δm_Λ, low p_T.

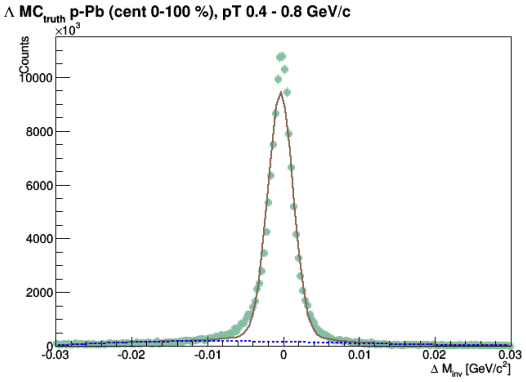

(b) MC_{truth} Δm_Λ, low p_T.

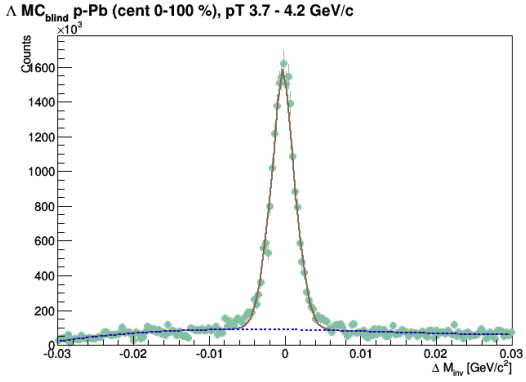

(c) MC_{blind} Δm_Λ, intermediate p_T.

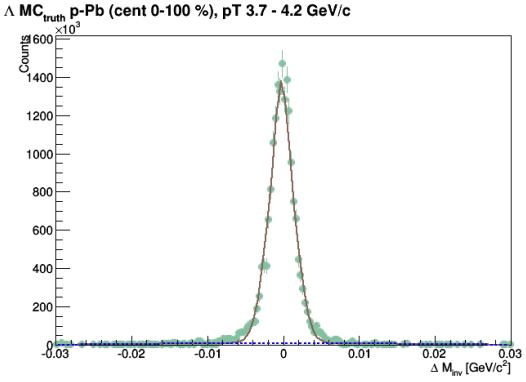

(d) MC_{truth} Δm_Λ, intermediate p_T.

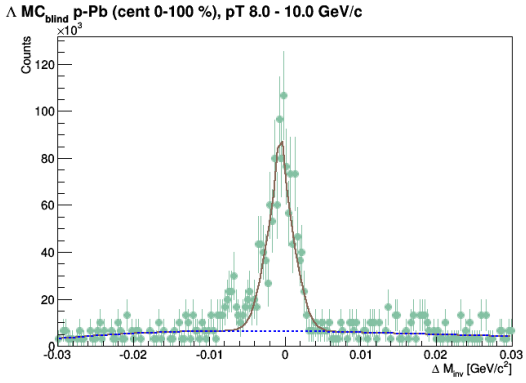

(e) MC_{blind} Δm_Λ, high p_T.

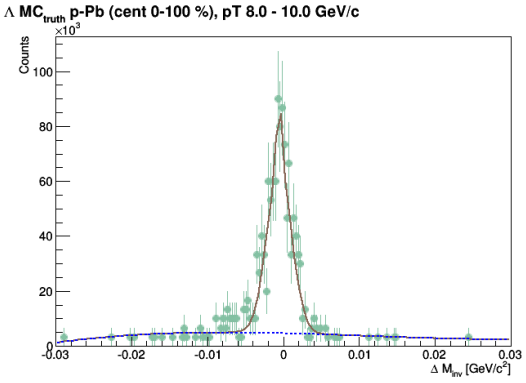

(f) MC_{truth} Δm_Λ, high p_T.

Figure 20: The MC_{blind} (left) and MC_{truth} (right) Δm for low ($0.4 < p_T < 0.8$ GeV/c), intermediate ($3.7 < p_T < 4.2$ GeV/c) and high ($8.0 < p_T < 10.0$ GeV/c) p_T.

5.5.1 Background Subtraction

When the invariant mass difference, Δm, for V^0 candidates is constructed, the spectrum contains some background, as seen on the left in Fig. 19 and 20. This background is the result of contributions from, e.g., wrongly associated tracks that do not originate from a V^0 decay or particles of similar mass that have decayed with a V^0-like topology. To be able to work with a clean signal, it is necessary to subtract the background from the mass spectrum. In this analysis, this was done in two ways:

1. Calculating the sum of the areas of the two sidebands, by integration, and subtracting this from the total area (peak and background) in the peak region. For K^0_S the peak was estimated to lie within the region $-0.015 \leq \Delta m \leq 0.015$ GeV/c^2 and the sidebands were calculated from $\Delta m \geq -0.03$ GeV/c^2, on the left-hand side, up to $\Delta m \leq 0.03$ GeV/c^2, on the right-hand side. For Λ the peak is narrower, so the peak was estimated to lie within $-0.008 \leq \Delta m \leq 0.008$ GeV/c^2, whereas the sidebands were calculated from $\Delta m \geq -0.016$ GeV/c^2, on the left-hand side, up to $\Delta m \leq 0.016$ GeV/c^2, on the right-hand side[9]. This method is expected to work well for cases when the background is approximately linear for the considered region.

2. Fitting one function to the total spectrum and one to the background and subtracting the background function from the total fit. The fit consists of two Gaussian functions, for the peak, and a 3^{rd} degree polynomial, for the background.

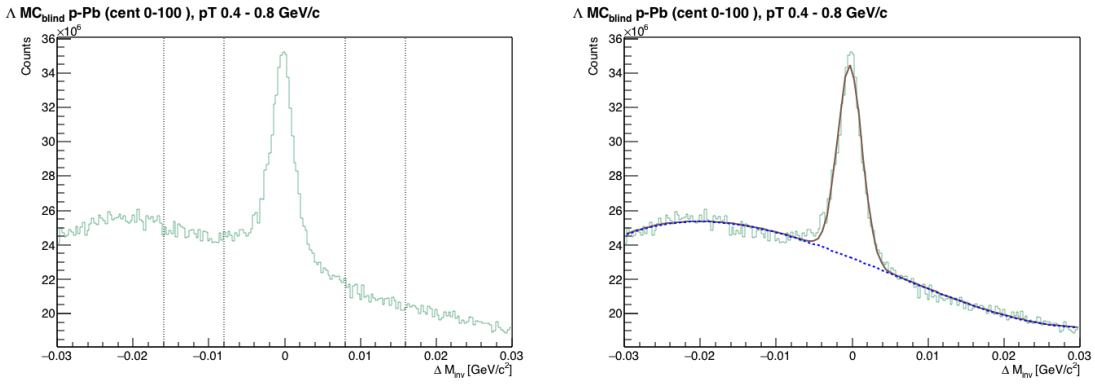

(a) Sideband subtraction method. (b) Fit method.

Figure 21: The two methods used for background subtraction.

A graphical represetation of the two methods is given in Fig. 21, where (a) shows the sideband method, where the sidebands are marked by two vertical lines on either

[9]By dividing the area into four equally sized segments, where the two inner segments represent the peak region, the background can be subtracted so that only the signal remains. This requires the region around the peak to be made narrow enough for little, or no, background to be included, but wide enough to cover the whole peak.

side of the peak and (b) shows the fit method, where the total fit is plotted together with the background fit.

The signal obtained from the background subtracted, or fitted, MC_{blind} is then compared to that of MC_{truth}, which has negligible background. If the two are comparable, it means that the method is robust, and can reliably be used on real data. The results of these methods are shown in Fig. 22 and 23.

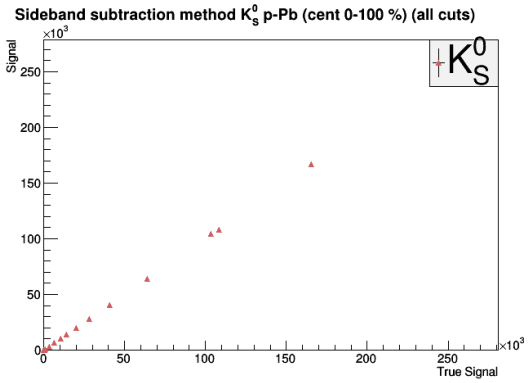

(a) K_0^S. Signal of MC_{blind} vs signal of MC_{truth}, using the sideband subtraction method.

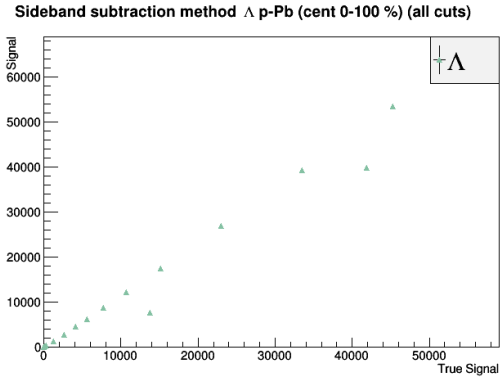

(b) Λ. Signal of MC_{blind} vs signal of MC_{truth}, using the sideband subtraction method.

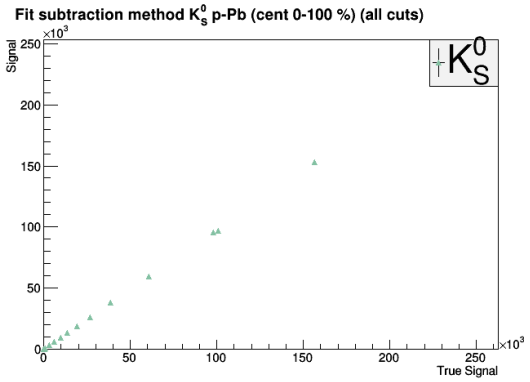

(c) K_0^S. Signal of MC_{blind} vs signal of MC_{truth}, using the fit method.

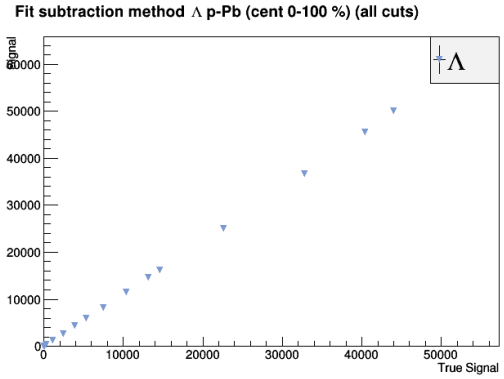

(d) Λ. Signal of MC_{blind} vs signal of MC_{truth}, using the fit method.

Figure 22: Comparison of the extracted signals from MC_{blind} and MC_{truth} using the sideband subtraction method for (a) K_S^0 and (b) Λ. Note that in both cases the plots follow a linear curve, indicating that the MC_{blind} signal after the background subtraction matches that of MC_{truth}. (c) and (d) show the extracted signals using the fit method. It seems that the fit works well for K_0^S, as well as Λ, which indicates that both methods are reliable for extracting the signal.

Another way to tell if the methods are robust is to check exactly how much the two areas displayed in Fig. 22 differ from one another. This is shown in Fig. 23 and is done by calculating $(MC_{blind} - MC_{truth})/MC_{blind}$, i.e. the difference between the derived MC_{blind} and MC_{truth} signals, normalized to MC_{blind}.

Figure 23 shows that the sideband subtraction method is overall more robust and with smaller errors than the fitting method for extracting the V^0 signals throughout

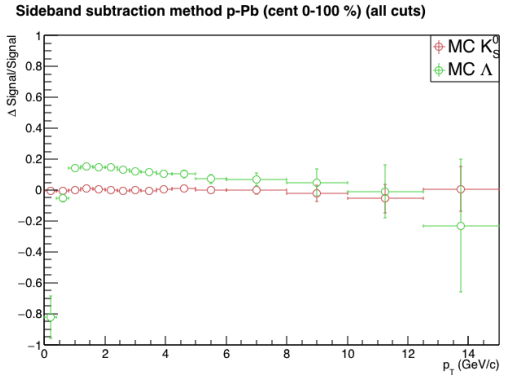

(a) Normalized signal difference using sideband subtraction.

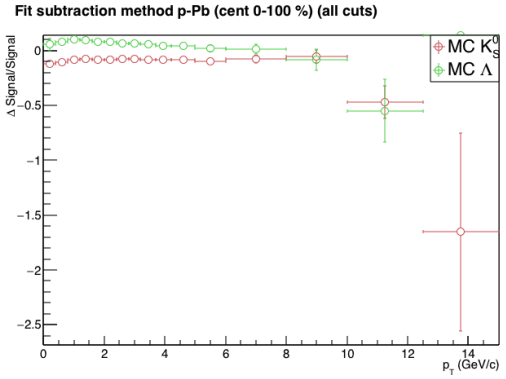

(b) Normalized signal difference using fits.

Figure 23: $(MC_{blind} - MC_{truth})/MC_{blind}$ for the two methods.

the p_T spectrum, especially at high p_T where the fit fails due to low statistics. For the Λ particle, however, the sideband method fails at low p_T (see Fig. 23a), while the fit method in this p_T region works quite well. This was as expected since the background seen in Fig. 20 is not linear for the whole Δm_Λ range. As expected, there is a $10 - 20\%$ discrepancy between the MC_{blind} and MC_{truth} for Λ, since the feeddown has not yet been corrected for.

Continuing from here, the results from the sideband subtraction will be used for the rest of the analysis, since it in general seems to be the more stable way of calculating the V^0 signals.

5.5.2 The p_T Spectrum

Having subtracted the background and applied all the cuts, the next step is to examine the resulting p_T spectra. The p_T spectra for K^0_S and Λ are presented in Fig. 24. For the MC_{blind} and MC_{truth} spectra an efficiency correction has been made. Additionally for Λ MC_{blind} a feeddown correction was made, by subtracting the feeddown fraction in Fig. 15 from the uncorrected MC_{blind} p_T spectrum.

In Fig. 24 the efficiency corrected spectra of MC_{blind} and MC_{truth} are presented. Seeing that the MC_{blind} and MC_{truth} spectra now seem to agree very well, means that the analysis method is reliable and can with certainty be used on real data. Ideally, the corrected spectrum should match that of MC_{gen}. In this analysis, however, a slight discrepancy between the two spectra was found but, due to lack of time, this was not further investigated.

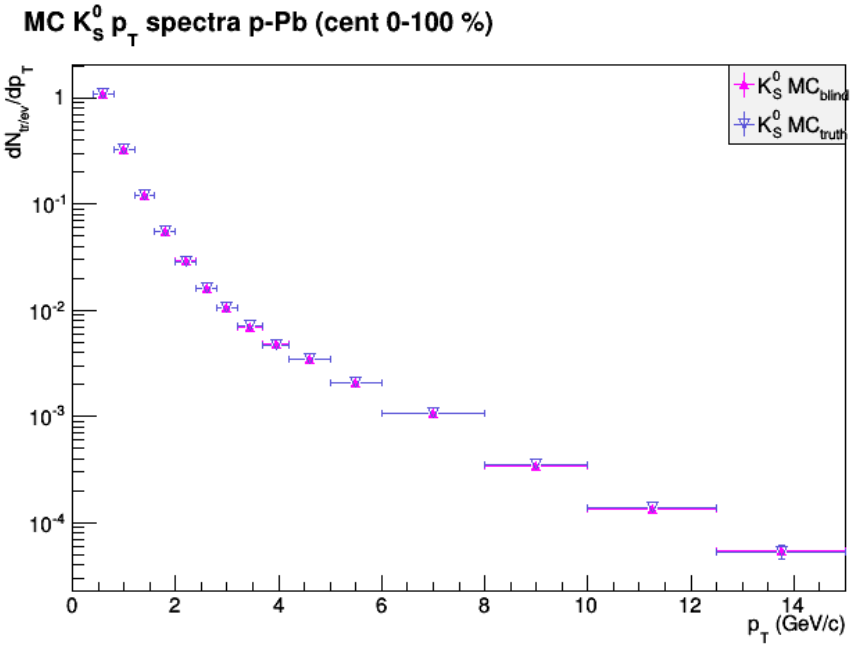

(a) MC K^0_S.

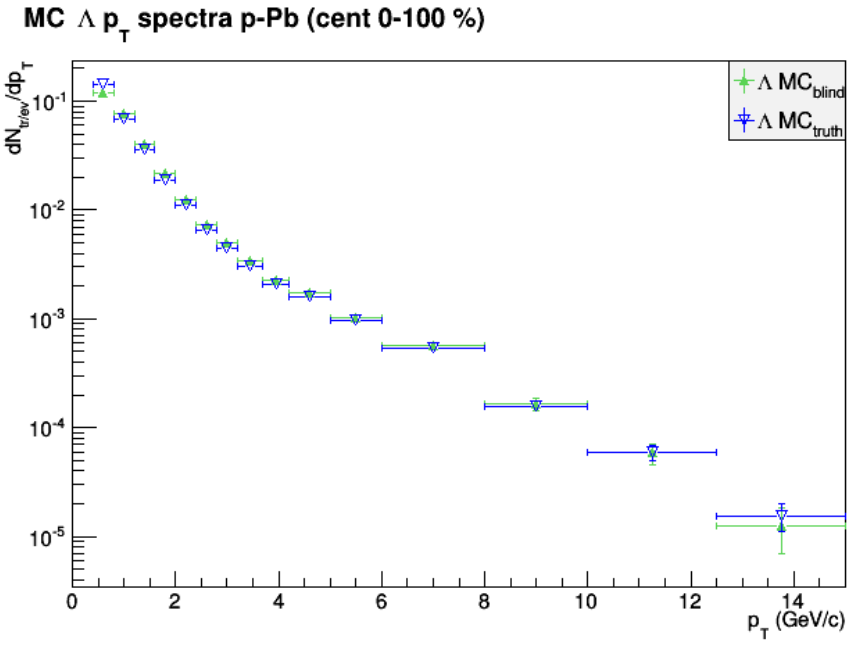

(b) MC Λ.

Figure 24: p_T spectra of MC$_{blind}$, MC$_{truth}$ and MC$_{gen}$ (not normalized).

5.6 The 5.02 TeV p-Pb Data

Upon completing the MC study and verifying that the method works, it is now time to reproduce the analysis with data from real collision. For the data analysis, the same cuts were applied as for MC. The Δm for the data, in three different p_T bins, is shown for K^0_S and Λ in Fig. 25 and 26, respectively. Just as for the simulated MC_{blind} data, a background subtraction, using the sideband method, is done in order to reduce the background and obtain a clean signal of V^0 particles. After this an efficiency correction is performed on the constructed p_T spectra using the efficiency obtained from the MC, and for the Λ particle the feeddown fraction, calculated in the MC analysis, is subtracted from the spectrum. The p_T spectra of the Λ and K^0_S particles, after all cuts and corrections have been applied, are shown in Fig. 27, together with MC_{truth} (also seen in Fig. 24).

Comparing the data spectra to (the un-normalized) MC_{truth}, it is clear that the signal throughout the p_T spectra is higher for the real data, which means that the MC model underestimates the particle yields. The shapes of the spectra, however, seem to be quite well reproduced by the model.

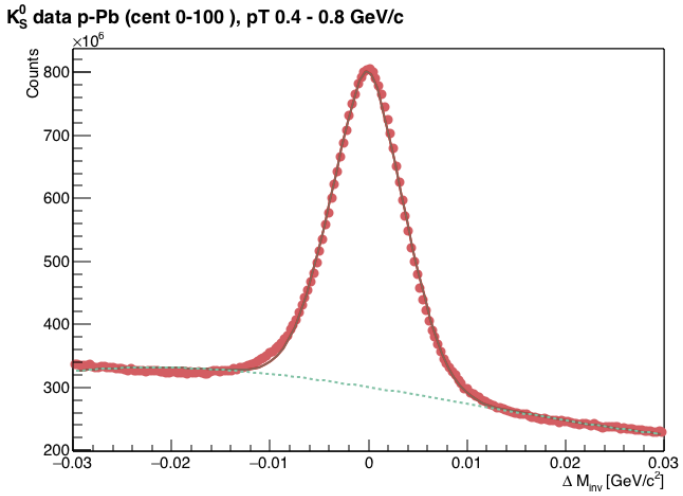

(a) Data $\Delta m_{K^0_S}$, low p_T.

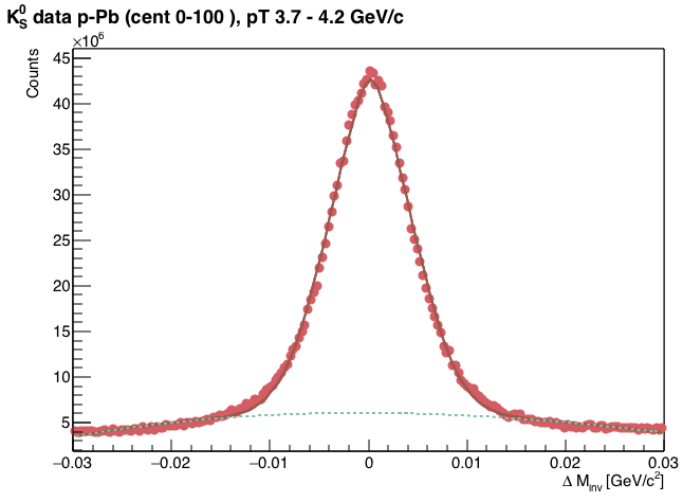

(b) Data $\Delta m_{K^0_S}$, intermediate p_T.

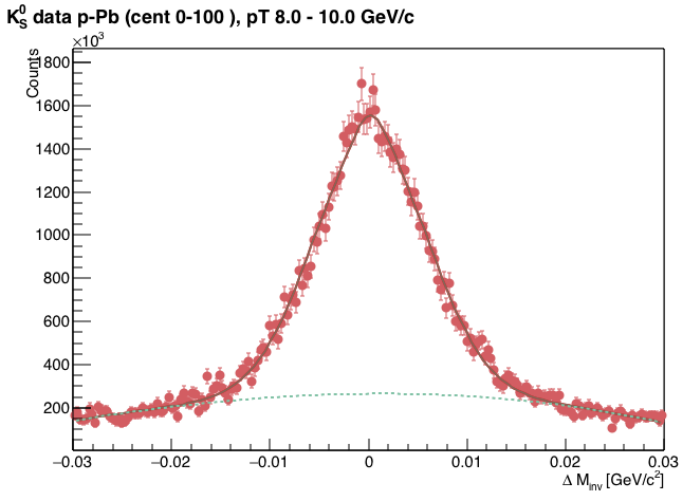

(c) Data $\Delta m_{K^0_S}$, high p_T.

Figure 25: K^0_S Δm for low ($0.4 < p_T < 0.8$ GeV/c), intermediate ($3.7 < p_T < 4.2$ GeV/c) and high ($8.0 < p_T < 10.0$ GeV/c) p_T. The dashed line represents the background fit.

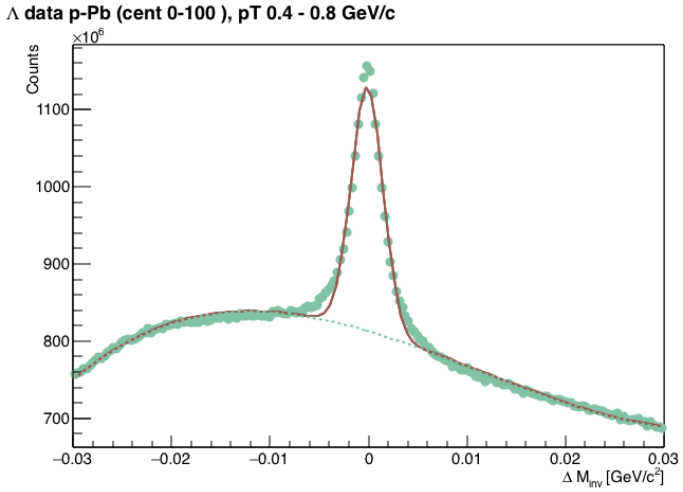

(a) Data Δm_Λ, low p_T.

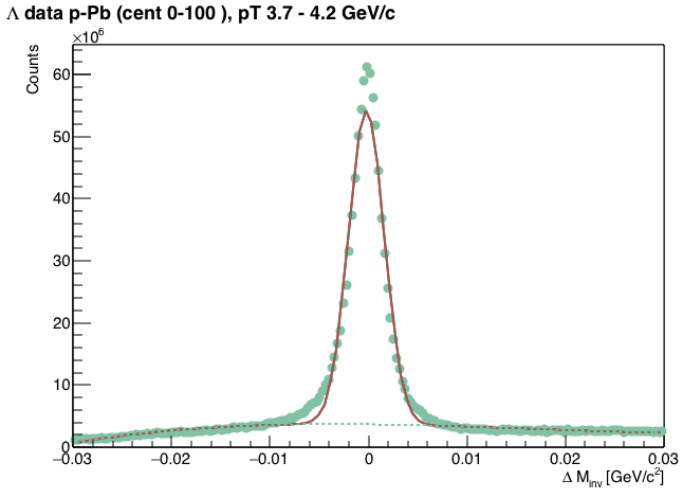

(b) Data Δm_Λ, intermediate p_T.

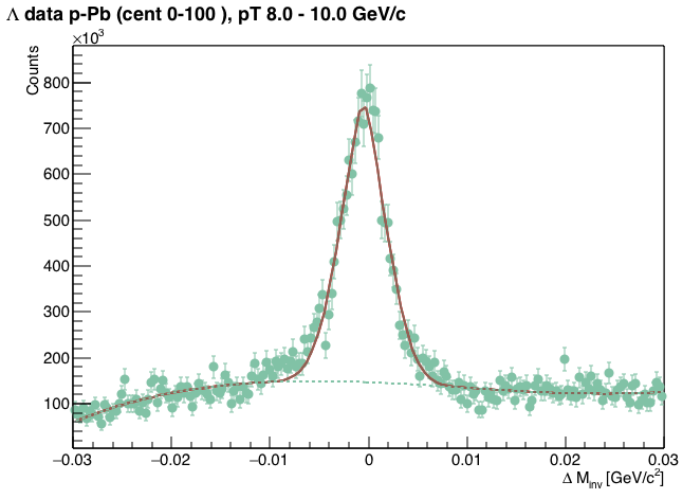

(c) Data Δm_Λ, high p_T.

Figure 26: Λ Δm for low ($0.4 < p_T < 0.8$ GeV/c), intermediate ($3.7 < p_T < 4.2$ GeV/c) and high ($8.0 < p_T < 10.0$ GeV/c) p_T. The dashed line represents the background fit.

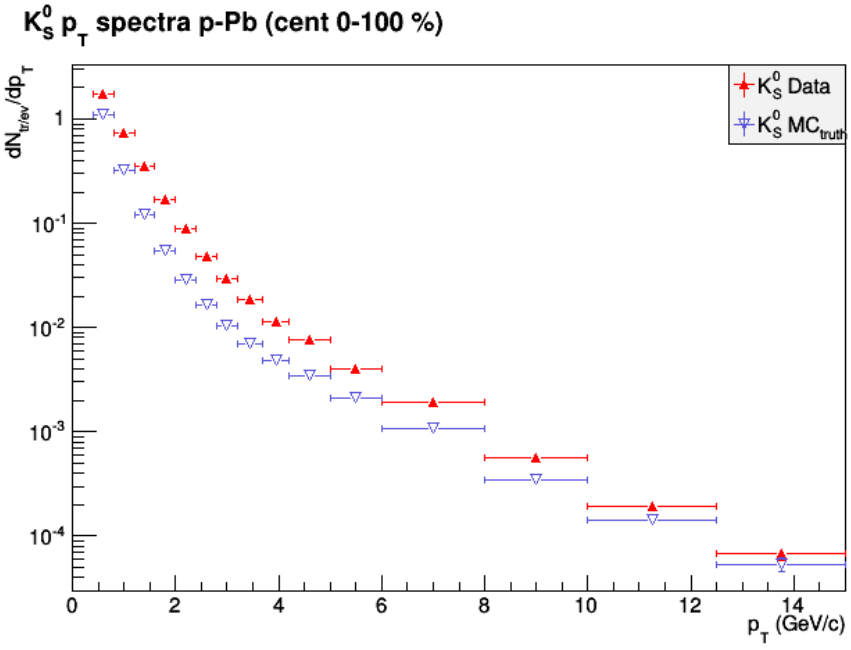

(a) K^0_S p_T.

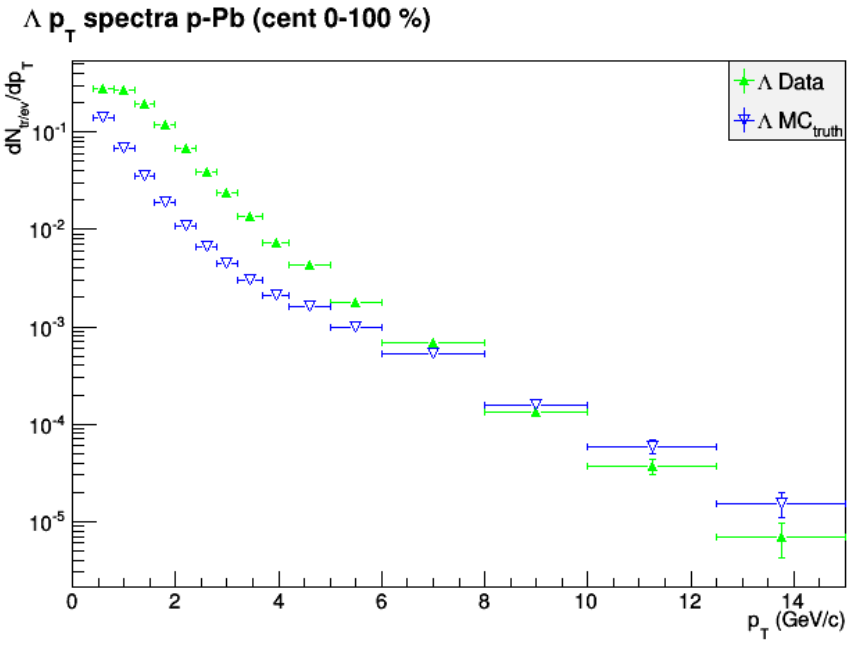

(b) Λ p_T.

Figure 27: K^0_S and Λ p_T spectra (MC$_{truth}$ not normalized).

6 Results and discussion

6.1 The nuclear modification factor R_{CP}

The analysis has been done for different centrality bins, to make it possible to compare the particle yields, especially, of the most central collisions to those of the most peripheral ones as well as performing qualitative physics studies without having the final absolute normalization of the spectra. A way to examine this is by calculating the so called R_{CP}, as discussed in section 3.2.5. Please note that N_{coll} – the estimated amount of binary collisions between the nucleons – is accounted for in the R_{CP} ratio. The values of N_{coll} are, however, very biased in p-Pb and thus not completely reliable, something well known and taken into consideration by ALICE [12]. The R_{CP} is shown in Fig. 28 for (a) K^0_S and (b) Λ. The ratio is plotted for all the different centrality bins; $0-20\%$, $20-40\%$, $40-60\%$, and $60-100\%$ (the last bin plotted for reference).

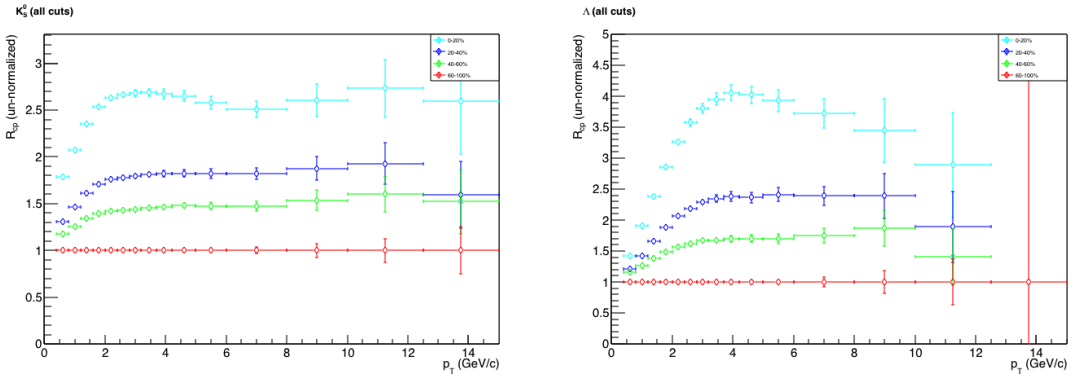

(a) The K^0_S R_{CP} ratio.

(b) The Λ R_{CP} ratio.

Figure 28: K^0_S and Λ R_{CP}.

Looking at these plots, it is possible to deduce a bit of information on the creation of V^0 particles; the number of V^0's produced in a collision increases for more central collisions (where there is a bigger overlap between the colliding nuclei) and the number of Λ particles, at mid-p_T, increases more with centrality than the number of K^0_S particles. The question is now, how the particle yields of the two particles, at different centralities, change in relation to each other. This can be examined by looking at the yield ratio between the Λ and K^0_S particles, i.e. the Λ/K^0_S.

The N_{coll} values for different centralities are presented in Table 2 and the number of tracks per centrality bin is can be seen in Fig. 29.

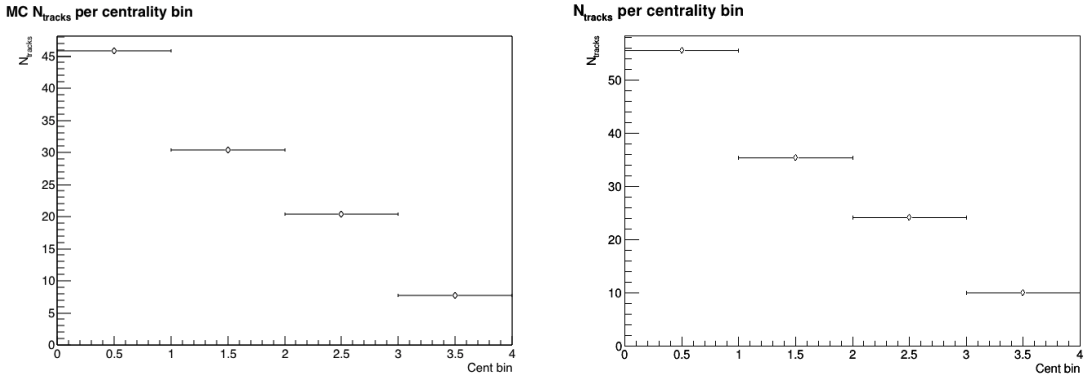

(a) MC. (b) Data.

Figure 29: The average number of reconstructed tracks ($|\eta| < 0.8$) per collision for each centrality bin.

Table 2: Values of N_{coll} for different centralities.

Centrality	N_{coll}
$2 - 20\%$	$11.3 \pm 0.6 \pm 0.9$
$20 - 40\%$	$9.6 \pm 0.2 \pm 0.8$
$40 - 60\%$	$7.1 \pm 0.3 \pm 0.6$
$60 - 80\%$	$4.3 \pm 0.3 \pm 0.3$
$80 - 100\%$	$2.1 \pm 0.1 \pm 0.2$

6.2 The Λ/K^0_S yield ratio

The aim of this analysis has been to investigate the strangeness baryon/meson ratio, Λ/K^0_S, for central as well as peripheral p-Pb collisions. The result of this is presented in Fig. 30. Just as for Pb-Pb this shows a rise at low p_T due to an increase in radial flow as well as the hard scattering effects at high p_T. It also shows a clear difference, at intermediate p_T, between particle yield ratios of the most central and the most peripheral collisions, which is consistent with the one seen in Pb-Pb collisions. These results agree well with the published results from ALICE (see Fig. 31, left). Comparing the left figure (p-Pb) to the right one (Pb-Pb) the main thing to notice is the difference in height of the ratios from central p-Pb and central Pb-Pb, due to the fact that the effect is much more enhanced for Pb-Pb. However, the overall features of the p-Pb spectrum are similar to those of Pb-Pb and show a consistency with the QGP production in Pb-Pb collisions. To verify that no Λ/K^0_S enhancement occurs at high p_T, I have done this analysis for $p_T \leq 15$ GeV/c, where hard scattering seems to be persistently dominating for $p_T > 8$ GeV/c.

In order to determine whether what is seen in the Λ/K^0_S is a suppression of K^0_S's or if it is indeed an enhancement of Λ's, the ratios between the yields in each centrality bin and the minimum bias[10] are examined. In Fig. 32 a larger difference is seen between the central and peripheral yields of Λ than of K^0_S. This means that the Λ particle gets a larger push in momentum in central collisions than the K^0_S, an

[10]By minimum bias is meant the yields from all centralities, i.e. $0 - 100\%$.

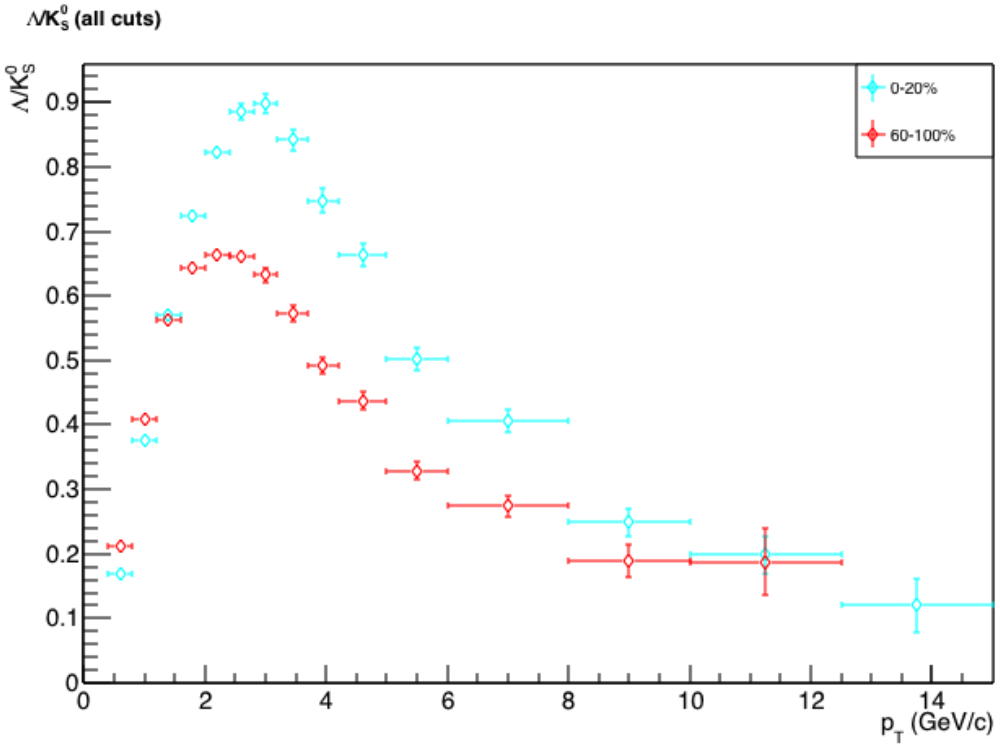

Figure 30: The Λ/K^0_S ratio.

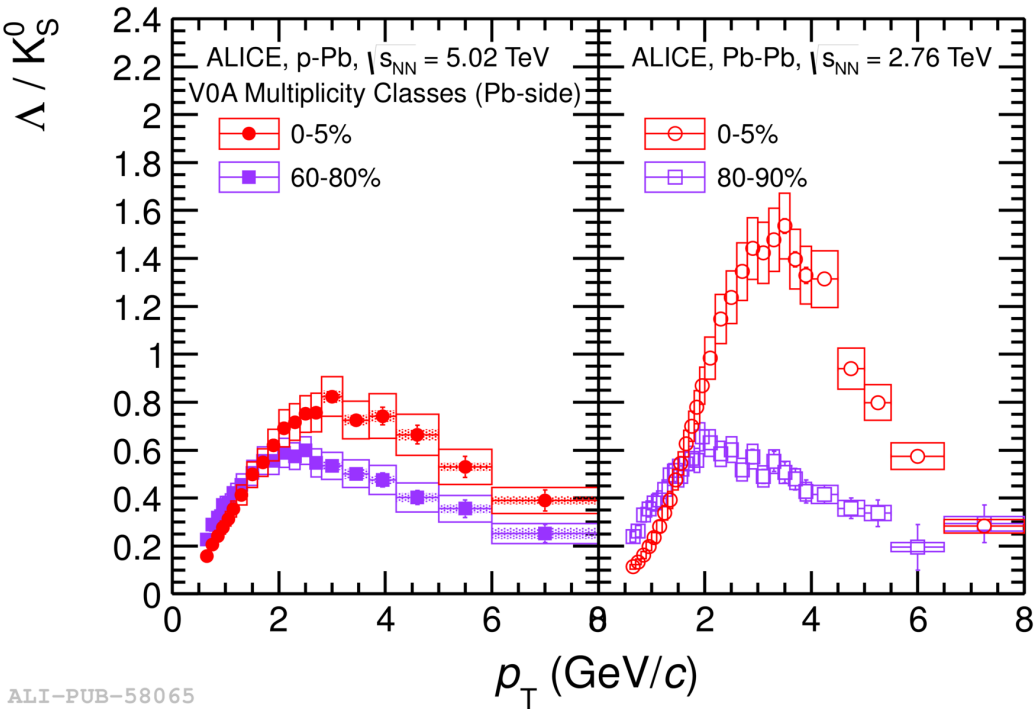

Figure 31: Lambda-to-K0s ratio vs. p_T. Figure and caption taken from [33].

effect which becomes more obvious in the mid-p_T region where there is an overall lower amount of particles. However, there also seems to be a slight suppression of Λ's in peripheral collisions, at intermediate p_T. For peripheral collisions – just as for pp – pronounced effects of QGP are not expected to be observed and hence nor effects of radial flow. Thus, hadrons consisting of two quarks (mesons) and with lower mass (which are easier to create) appear more abundantly throughout the p_T spectrum.

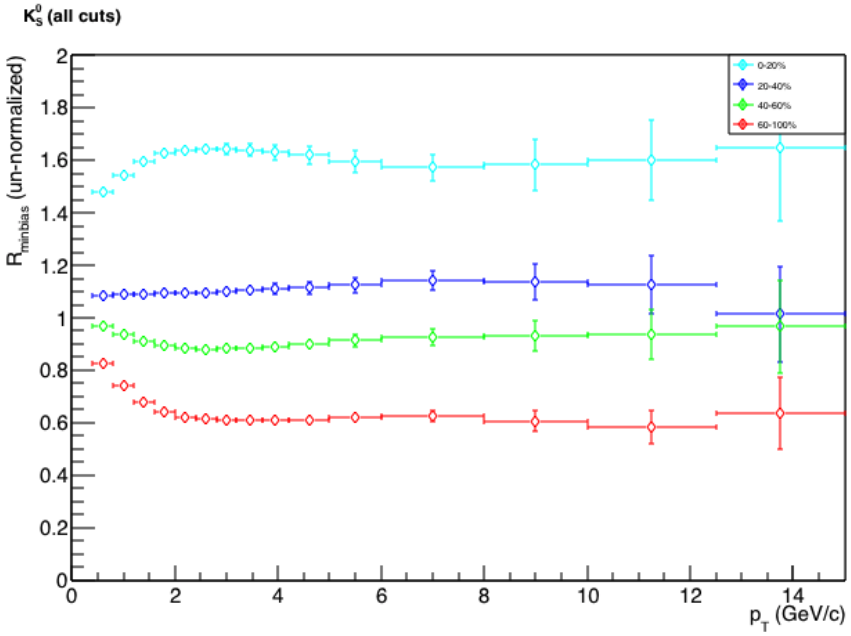

(a) K^0_S.

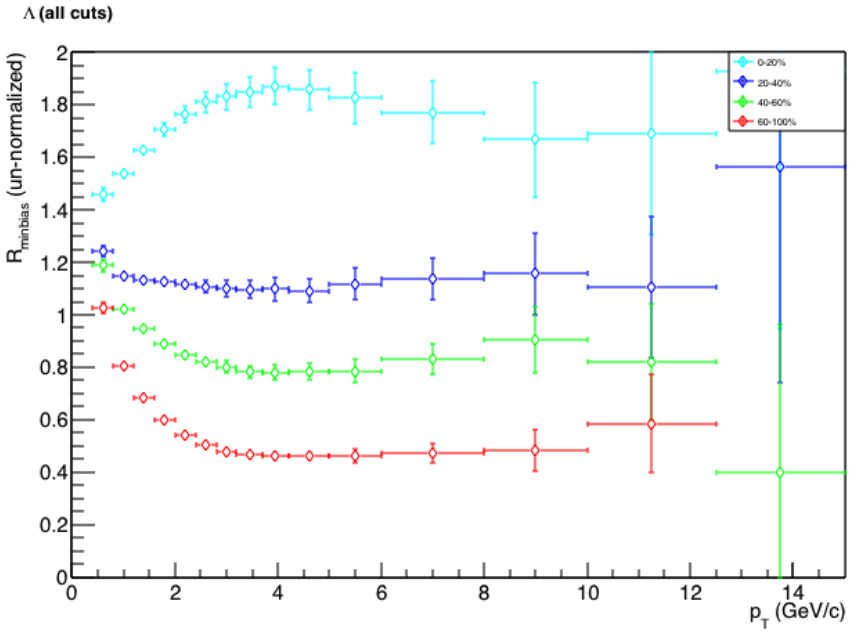

(b) Λ.

Figure 32: K^0_S and Λ to minimum bias ratio.

7 Conclusions

The aim of this analysis was to examine the production of K^0_S and Λ particles in p-Pb collisions for different collision centralities. The results were obtained by separating the signal from the background in the Δm spectra, using sideband subtraction around the peak region. For the Λ/K^0_S ratio, a difference was observed in the mid-p_T region between the yield ratios from central collisions $(0-20\%)$ and peripheral collisions $(60-100\%)$, which is in agreement with published results from ALICE. The observed behavior is similar to that seen in Pb-Pb collisions, where it is interpreted as due to the collective expansion of the QGP.

To further narrow down the origin of this phenomenon two different directions were taken in this study. Firstly, the ratio was examined for $p_T \leq 15$ GeV/c (increasing the range previously studied by ALICE), in order to assure that no collective effects are observed at high p_T. Secondly, a ratio of spectra in different centrality classes was done for the K^0_S and Λ separately. This showed that, while both K^0_S and Λ particles are enhanced at intermediate p_T in high multiplicity collisions, the magnitude of the enhancement is larger for the Λ particles. Both these observations add evidence to the suggested QGP explanation, i.e. an effect of quark recombination and/or radial flow.

References

[1] http://aliceinfo.cern.ch/TPC/node/7

[2] T. Richert "Λ/K^0_S Associated with a Jet in Central Pb-Pb Collisions at $\sqrt{s_{NN}} = 2.76$ TeV Measured with the ALICE Detector" (Faculty of Science, Lund University, Lund, 2016)

[3] , https://en.wikipedia.org/wiki/Standard_Model#/media/File:Standard_Model_of_Elementary_Particles.svg

[4] http://www2.ph.ed.ac.uk/~muheim/teaching/np3/lect-qcd.pdf

[5] http://homepages.uni-regensburg.de/~sow28704/ftd_lqcd_ss2012/ftd_lqcd_ss2012.html

[6] http://hyperphysics.phy-astr.gsu.edu/hbase/Forces/couple.html

[7] http://home.thep.lu.se/~torbjorn/talks/durham09.pdf

[8] http://fias.uni-frankfurt.de/~hossi/Bilder/BR/Plotl/Phasendiagram.jpg

[9] A. Dainese, "Review on Heavy-Ion Physics" (Il Nuovo Cimento, Padova, 2010), p. 3

[10] http://www.hep.shef.ac.uk/edaw/PHY206/Site/2012_course_files/phy206rlec7.pdf

[11] http://cerncourier.com/cws/article/cern/53089

[12] ALICE Collaboration, "Centrality Dependence of Particle Production in p-Pb collisions at $\sqrt{s_{NN}} = 5.02$ TeV" (CERN-PH-EP-2014-281, 2014), p. 1-3

[13] N. van der Kolk, " To flow or not to flow: A study of elliptic flow and nonflow in proton-proton collisions in ALICE" (Utrecht University, Utrecht, 2012) p. 18

[14] https://aliceinfo.cern.ch/Figure/node/8914

[15] National Research Council. "Nuclear Physics: Exploring the Heart of Matter." (Washington, DC: The National Academies Press. doi: 10.17226/13438., 2013.), p. 85

[16] https://aliceinfo.cern.ch/Figure/node/4798

[17] K. Werner, "Lambda-to-Kaon Ratio Enhancement in Heavy Ion Collisions at Several TeV" (Phys. Rev. Lett. 109, 2012)

[18] C. Fabjan and J. Schukraft, "The Story of ALICE: Building the Dedicated Heavy Ion Detector at LHC" ('The Large Hadron Collider: A marvel technology', EPFL-Press, Lausanne, 2009), p. 3-16

[19] http://aliceinfo.cern.ch/Public/en/Chapter2/Chap2_TPC.html

[20] http://aliceinfo.cern.ch/Public/en/Chapter2/Chap2_TRD.html

[21] www-alice.gsi.de/trd/intro.html

[22] http://aliceinfo.cern.ch/Public/en/Chapter2/Chap2_TOF.html

[23] http://aliceinfo.cern.ch/ArtSubmission/node/716

[24] http://cerncourier.com/cws/article/cern/53084

[25] http://www.quantumdiaries.org/2010/10/13/
meet-the-alice-electromagnetic-calorimeter/

[26] http://aliceinfo.cern.ch/Public/en/Chapter2/
Page3-subdetectors-en.html

[27] http://iopscience.iop.org/article/10.1088/1742-6596/160/1/012045/
pdf

[28] ALICE Collaboration, "Technical Design Report on Forward Detectors: FMD, T0 and V0" (CERN-LHCC-2004-025, 2004), p. 5-6, 55-56, 94

[29] http://aliceinfo.cern.ch/Public/en/Chapter2/Chap2_ZDC-en.html

[30] E. Cuautle et. al, "ACORDE, The ALICE Cosmic Ray Detector" (Proceedings of the 30th International Cosmic Ray Conference, Vol. 5 (HE part 2), Mexico City, 2008), p. 1201

[31] https://aliceinfo.cern.ch/Notes/sites/aliceinfo.cern.ch.
Notes/files/notes/analysis/ddobrigk/2012-Oct-09-analysis_
note-V0AnNote18.pdf

[32] https://root.cern.ch/

[33] https://aliceinfo.cern.ch/Figure/node/5070